Hierarchical topology optimization for bone tissue scaffold

Emily Gogarty

Department of Mechanical Engineering

McGill University

Montreal Canada

A thesis submitted to McGill University in partial fulfillment of the requirements for the degree of Master of Engineering.

August 2014

Abstract

The use of scaffold materials for reconstructive orthopaedics is a strong candidate for promoting tissue regeneration while addressing both mechanical and biological constraints. A scaffold's microarchitecture can be specifically tailored to locally match specific properties of the host tissue resulting in a biologically fixed implant. As such, the use of an optimized graded scaffold mitigates otherwise present issues causing implant failure, such as bone resorption and shear stress at the implant interface.

A 2D hierarchical topology optimization technique has been developed here for the design of a cellular bone tissue scaffold that mimics the stiffness of the surrounding bone while maximizing permeability for bone ingrowth. The procedure involves sequentially optimizing material layout at two scales: 1) the material distribution of the implant, and 2) the cellular material used in its construction. In the first stage, an optimal material distribution is obtained for the implant such that the stiffness of the structure matches that of bone. In the second stage, the optimal relative density distribution from the previous stage is used to interpolate target material properties at each location of the implant domain. Target matching topology optimization is used to obtain unit cells with desired stiffness and maximum permeability throughout the implant. The procedure is currently developed in 2D and can be extended to produce clinically relevant 3D implant models.

A 2D bone fracture fixation plate is designed as a demonstration of the proposed methodology, where an in-plane loading scenario is assumed. The plate is optimized at both the material and cellular level to achieve target stiffness and permeability properties based on physiological requirements. It is shown that by integrating multi-objective optimization with multi-scale topology optimization, a bone tissue implant can be created that is both mechanically optimal and conducive to bone tissue regeneration.

Abrégé

L'utilisation de matériaux d'échafaudage pour l'orthopédie reconstructive est un excellent candidat pour la promotion de la régénération des tissus tout en s'occupant des contraintes mécaniques et biologiques. La microarchitecture de l'échafaudage peut être spécifiquement conçue pour égaliser les propriétés locales spécifiques du tissu de l'hôte résultant en un implant biologique fixe. En tant que tel, l'utilisation d'un échafaudage gradué optimisé atténue les problèmes autrement présents qui provoquent l'échec de l'implant, telles que la résorption osseuse et la contrainte de cisaillement à l'interface de l'implant.

Une technique 2D d'optimisation hiérarchique de la topologie a été développée ici pour la conception d'un échafaudage pour tissu osseux qui imite la rigidité de l'os qui l'entoure, tout en maximisant sa perméabilité pour la croissance osseuse. Le procédé consiste à optimiser séquentiellement la disposition de matériau à deux échelles: 1) la distribution de matériel de l'implant, et 2) le matériau cellulaire utilisée dans sa construction. Dans la première étape, une distribution de matériau optimal est obtenue pour l'implant de sorte que la rigidité de la structure correspond à celle de l'os. Dans la deuxième étape, la distribution optimale de densité relative de l'étape précédente est utilisée pour interpoler les propriétés matérielles ciblées à chaque emplacement du domaine de l'implant. Optimisation topologique d'adaptation de cible est utilisée pour obtenir des cellules élémentaires avec rigidité souhaitée et la perméabilité maximale tout au long de l'implant. Le procédé est actuellement développé en 2D et peut être étendu afin de réaliser des modèles d'implants 3D cliniquement pertinentes.

Une plaque 2D pour la fixation des fractures de l'os est conçue comme une démonstration de la méthodologie proposée, où un scénario de chargement complètement dans le plan est présumé. La plaque est optimisée à la fois au niveau matériel et au niveau cellulaire pour obtenir la raideur et les propriétés de perméabilité ciblées selon les exigences fonctionnelles. Ainsi, en intégrant l'optimisation multi-objective avec l'optimisation topologique multi-échelle, un implant de tissu osseux peut être créé qui est à la fois mécaniquement optimal et favorable à la régénération des tissus osseux.

Acknowledgements

I would like to express my gratitude to my supervisor Damiano Pasini for his continuous support and guidance throughout the course of this work. I am very grateful for the opportunity to have been a part of the Pasini Lab, with particular thanks to Kishan for his infallible debugging skills and generosity with time and advice. Thank you especially to Rob, my family, and friends for the endless encouragement and help in keeping everything in perspective.

Table of Contents

List of Tables

List of Figures

Chapter 1: Introduction

1.1 Bone Tissue

Bone tissue serves four important functions in the body: 1) protection of organs, 2) structural support of muscle attachment for locomotion, 3) generation of red and white blood cells, and 4) calcium and other ion storage. It is apparent that bone serves a large range of purposes, and any damage to the skeletal system has widespread effects [1]. Damage due to disease, abnormal development, or trauma can be addressed through artificial bone tissue scaffolds. The design of such scaffolds is a multidisciplinary area with much research potential. Currently, technological and scientific advances in areas such as additive manufacturing and biomaterials have allowed for the design and manufacturing of bone tissue scaffolds to become a reality. The scope of this thesis is to first review the technology currently used to repair and replace bone, and then to propose a design methodology to improve upon the current state of the art. It is therefore essential and appropriate to discuss the biology of bone before entering into the details of the design of a bone tissue scaffold.

1.1.1 Structure and composition

Bone is a composite material made up of an organic phase and inorganic phase, with a varying composition depending on anatomic site, age, health and presence of disease. The organic phase is a fibrous matrix made up of protein (90% collagen). The matrix is filled with the inorganic phase, primarily hydroxyapatite, and serves as a reservoir of calcium and phosphate. The inorganic phase is primarily responsible for bone stiffness. The organic phase has a low modulus of elasticity, good tensile strength, and relatively poor compressive strength. The combination of the two phases results in an anisotropic material which is strongest in compression [2].

On the macroscopic level, the human skeleton consists of long bones, flat bones, and cuboid bones (femur, skull, and vertebrae respectively). The structure of bone can be divided into two categories: cortical and trabecular (also referred to as cancellous). The spongy trabecular bone is the most active component in growth and calcium regulation, and mechanically is best suited to resist compression loading. In adults, approximately 80% of bone is cortical and 20% is trabecular, percentages that vary throughout the body. Cortical bone is mainly located in the shafts of long bones and peripheral linings of flat bones [3]. The structural

arrangement of a bone can be described as a hollow tube or bilaminar plate of cortical bone, with trabecular "struts" reinforcing the architecture. The configuration of porous and cortical bone in this fashion minimizes the weight of the bone while still providing a large bearing area. This is advantageous at articular joints, for example, where a large area would reduce bearing stresses at the ends of long bones. In the case of the skull or iliac crest, this bone arrangement forms a low-weight sandwich. Essentially, the presence of cancellous bone allows for a reduced weight structure that contributes to satisfying mechanical requirements [4].

On the microscopic level, the structure type of bone can be either woven or lamellar. Woven bone is immature and unorganized, abundantly present in newborns and sites of bone formation. A remodeling process occurs to organize woven bone into a lamellar form, such as Haversian bone [3]. Adult cortical bone has a lamellar collagen fibre arrangement, which is densely packed and arranged both circumferentially and in a tubular formation (Figure 1). The tubular formation is made of concentric lamellae layers, forming an osteon. Each osteon surrounds a central Haversian canal which contains blood vessels. The osteons are arranged around branching blood vessels, oriented along the long axis of the bone. Because of this orientation, the osteons act as fibres reinforcing the long bone and are essential in resisting deformation. Figure 1 shows the components of bone tissue using the femoral head as an example to illustrate the hierarchical structure [2].
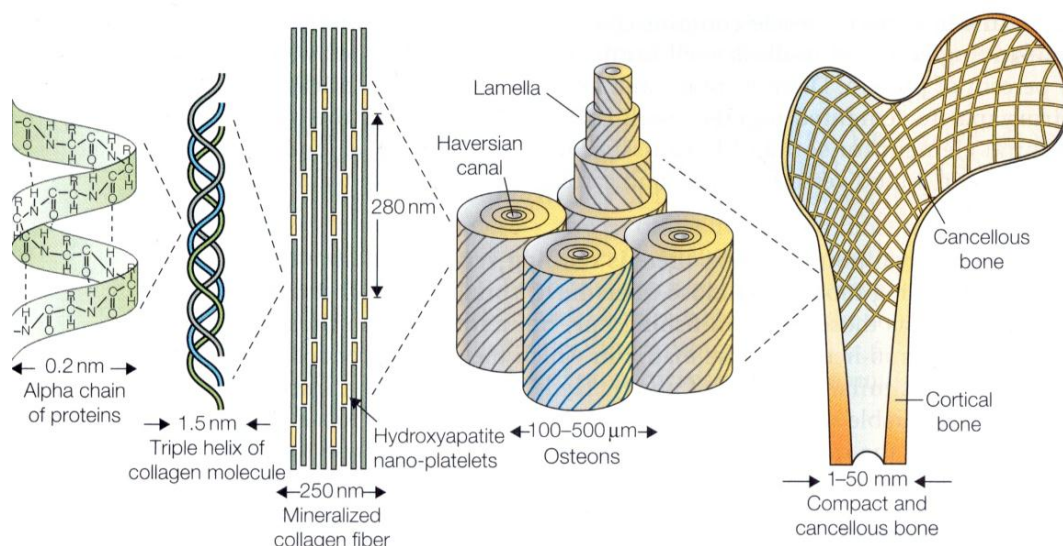
Figure 1: Hierarchical structure of bone in the femoral head [5].

Trabecular bone is approximately 25% as dense, 10% as stiff, and 500% as ductile as cortical bone. The mechanical properties of the two structural arrangements can differ by at least an order of magnitude. Trabecular bone can be described as open-celled porous foam, with an interconnected network of rod- and plate-like structures. This bone type is light, and acts as a scaffolding allowing room for blood vessels. Trabecular bone density varies greatly based on architecture, anatomic location, and age, directly impacting the mechanical properties of the tissue [2]. A predominantly rod-like network produces low-density, open cells, whereas a plate network gives higher density virtually closed cells. Technically, any bone with a relative density less than 0.7 is considered trabecular, and relative density typically ranges from 0.05 to 0.7 [4].

The biological composition of cortical and trabecular bone is very similar. However, the anisotropic structure of cortical bone consists of partial alignment of hydroxyapatite (fibre-like) in the longitudinal direction, making that the stiffer and stronger axis. Table 1 summarizes the mechanical properties of wet cortical bone, as reported by Gibson and Ashby. When bone is dried, elastic moduli increase and strength and strain to failure decrease. Wet cortical bone properties are used in all further analysis in this thesis.

Table 1: Mechanical properties of wet cortical bone [4].

Property	Value
Young's Modulus (GPa)	
Longitudinal	17.0
Radial	11.5
Tangential	11.5
Compressive Strength (MPa)	
Along	193
Normal	133
Tensile Strength (MPa)	
Along	148
Normal	49

Attempts have been made to determine the Young's modulus of single trabeculae using a number of techniques. These methods include direct mechanical testing (tension, bending, buckling), ultrasonic wave propagation in trabecular bone specimens, and finite element analysis. The solid cell wall properties for trabecular bone as reported by Gibson and Ashby are shown in Table 2. The properties shown in Table 2 are not that of a trabecular bone sample, but of individual trabeculae. In this table, the strength of individual trabeculae is gathered from the

assumption that the ratio of strength (σ) between cortical and trabecular bone is equal to the ratio of their respective moduli (E):

$$\sigma_t = \frac{E_t}{E_c}\sigma_c$$

Table 2: Solid cell wall properties for trabecular bone [4].

Property	Value
Young's Modulus (GPa)	12
Compressive Strength (MPa)	136
Tensile Strength (MPa)	105

1.1.2 Bone formation and remodeling

Two distinct mechanisms are responsible for the formation of the skeleton and maintenance of bones: intramembranous and endochondral bone formation. Intramembranous bone formation is the process by which flat bones, like the skull and scapula, are formed. Endochondral bone formation is the mechanism responsible for long bone formation growth. The characteristic process of this mechanism is the formation of cartilage preceding bone. The process begins with mesenchymal cells (MSCs) condensing and differentiating into chondrocytes that produce cartilage matrix. MSCs are progenitor cells that have the ability to differentiate into bone or cartilage forming cells. A dense fibrous layer known as the perichondrium covers this cartilage. Bone lengthening occurs from the chondrocyte division and matrix production. Chondrocytes within the periosteum enter their final stage and become hypertrophic chondrocytes, which are involved in the calcification of the matrix [1]. The cartilage matrix surrounding the enlarged chondrocytes becomes a site for calcification as the chondrocytes die. The result is calcified scaffolding for bone apposition. Concurrently, capillaries form within the perichondrium and the perichondrium differentiates into periosteum, responsible for delivering pre-osteoblasts. Ossification begins as capillaries and osteogenic cells invade the calcified cartilage and deposit osteoid, until almost the entire bone is ossified [3]. Remodeling through surrounding of the matrix continues to the point of remodeling the periosteal. The result is immature woven bone, which has many osteocytes. At this stage, bone remodeling occurs around the newly formed blood vessels, in the form of lamellar bone [1].

Bone remodeling is a dynamic and lifelong process of bone resorption (removal from the skeleton) and ossification (formation of new bone). The primary cells involved in bone remodeling are osteoblasts and osteoclasts, which specifically orchestrate resorption and ossification. Osteoblasts are responsible for the formation of new bone, whereas osteoclasts are responsible for digesting bone. Osteocytes are mature bone; osteoblasts become osteocytes. Bone cells (except osteoclasts) are highly interconnected by a network of cytoplasmic extensions, and together they make the basic multicellular unit of bone. All bone cells on the surfaces near a vascular supply are either active or inactive osteoblasts (bone lining cells). Osteocytes are found further away from the vascular supply, within the extracellular bone matrix [1]. It is hypothesized that the connected cellular network is the site of intracellular stimulus reception, signal transduction, and intercellular signal transmission for bone remodeling. Signal reception occurs in the osteocyte and the signal is transmitted by the osteoblast [6, 7]. The five distinct phases of bone remodeling are described below [1] and are illustrated in Figure 2.

  i.   Resting state – Inactive cells line the surface of bone. Osteocytes are trapped within the mineralized matrix.

 ii.   Activation – Stimuli (hormonal or physical) signal monocytes and macrophages to migrate to the site of modelling, which differentiate into osteoclasts.

iii.   Resorption – Osteoclasts remove organic/mineral components of bone to form a cavity in the bone. At a characteristic depth (60 microns from the surface in trabecular bone and 100 microns from the surface in cortical bone) resorption stops.

 iv.   Reversal – Osteoclasts disappear and macrophage-like cells smooth the surface of the site of resorption. This is achieved through the deposition of binding substance. Pre-osteoblasts begin to appear.

  v.   Formation – The cavity is filled in by differentiated osteoblasts and a new osteon begins to form. The osteon is formed by the deposition of osteoid followed by mineralization of the osteoid once the cavity is filled to 20 microns. At this point, the rate of mineralization is higher than the rate of mineral apposition (which still continues) until bone surface finally returns to its original state.
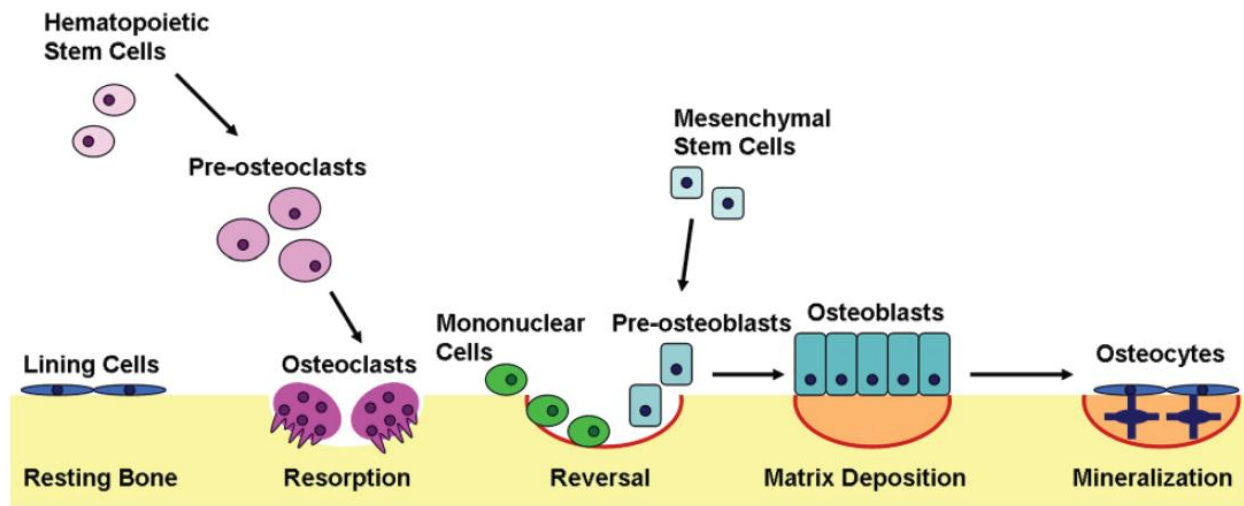
Figure 2: Bone remodeling process [8].

It has long been accepted that bone grows in response to stress, as stated most notably by Wolff et al. in 1869, but the mechanism is currently not fully understood. Wolff's law states the following: "Every change in the form and function of bone or of its function alone is followed by certain definite changes in the bone internal architecture, and equally definite alteration in its external conformation, in accordance with mathematical laws" [1]. Essentially, the skeleton adds or removes tissue in accordance with functional requirements with the purpose of reducing stress or resulting strain. For example, this phenomenon is observed in a scenario of low gravity: astronauts who spend an extended period of time in space experience reduced bone density.

It has been suggested that the piezoelectric nature of bone is a contributing factor to stress induced growth; that is, it generates electric potential when stressed. Additionally, it has been shown that there are non-mechanical factors involved in bone remodeling, including fluid flow within the bone. It is observed that prolonged immobilization induces bone weakness, whereas exercise increases bone strength. Aging has a high impact on the structure of trabecular bone, and density decreases significantly. This is partially due to the thinning of the cell walls and the remaining loss is attributed to the enlargement of circular perforations within the cell wall, to the point of complete loss of some cell walls [4]. As a consequence of decreased energy absorption, fracture risk increases. To counter decrease in mechanical properties due to age, bone remodels its geometry, thereby minimizing bending stress [2].

It is evident that trabeculae in cancellous bone develop along the principle stress trajectories when compared to principle stress trajectories in a similarly loaded solid, as supported by finite element analysis studies (Figure 3). It is a generally accepted theory that the density of cancellous bone is dependent on the magnitude of the applied load. It is observed that a comparison of micrographs of femoral head and density contour maps of the same femur show rod like structures (low density, open cell) in regions of low stress and plate like structures in regions of high stress (higher density, closed cell) [4]. Groups of trabecular lines are biologically developed to withstand tensile and compressive forces during gait (Figure 3). These trabecular patterns begin to develop at early stages of walking [2].
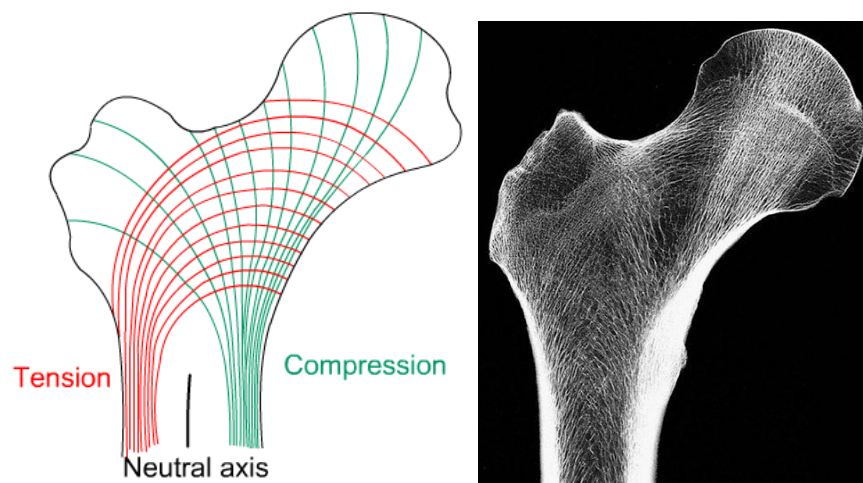
Figure 3: Computed stress lines of constant stress (left) [9], and X-ray image of proximal femur cross-section showing trabeculae trajectories (right) [10].

It is postulated that bone contains sensor cells that recognize mechanical strain and determine a corrective biological process for adjusting this value if it lies outside of an acceptable range. The general consensus of many investigators' models is that a mechanical stimulus below the acceptable threshold results in the removal of bone, whereas high mechanical stimulus results in the addition of new bone. It is suggested that the sensing cells are osteocytes, and can produce a signal proportional to the local mechanical loading. Furthermore, it is suggested that osteocytes sense fatigue damage and transmit signals to activate remodeling to remove the damage and prevent the occurrence of fracture fatigue [11].

There are some inconsistences between these current concepts and observations about bone remodeling. For example, it is observed that bone remodels with both excessively high and excessively low mechanical loading. This is contrary to the assumption that there is a signal produced by osteocytes proportional to mechanical stimulus. The new theory assumes that bone lining cells are always in a state in which they are inclined to activate remodeling, and mechanical loading within a specific range acts as an inhibitor to the transmission of this osteocytic signal [11]. Thus, in the cases of both under and over-loading, an inhibitory signal is restrained. Remodeling is initiated when signal generation declines due to reduced loading. Additionally, mechanical damage from over-loading, including micro-cracks and disturbance of the calcified matrix structure, may interfere with signal transmission by means of disconnecting cell to cell signal paths and by disturbing the flow of fluids over osteocytes. It is also hypothesized that mechanical damage can result in osteocyte apoptosis, which is death of the signal generating/transmitting cell. These mechanisms would be expected to inhibit osteocytic signals, leading to an increase in remodeling. A lower level of remodeling consistent with normal physiological loading is otherwise maintained [11].

The local mechanical environment is crucial in the determination of cell and tissue differentiation during bone remodeling. The mechanobiological response is the relationship between the mechanical environment and the cellular response, including molecular expression and cell differentiation. Depending on the type of mechanical loading, the mechanobiological response may result in the formation of bone, cartilage, or fibrotic tissue. The signals received by the osteoprogenitor cells will influence the tissue formed during development and healing [11]. The current mechanobiological model suggests that mechanical load acting on mesenchymal cells at the site of a defect would be directed to a specific response of differentiation into bone, cartilage, or fibrous tissue. In a model developed by Prendergast et al., it is assumed that the regulation of tissue regeneration is dependent on the magnitude of shear strain and fluidic velocity [12]. These factors should be considered in the design of a bone tissue scaffold, as its architecture would influence the mechanical environment upon implantation [11].

1.1.3 Bone as a cellular material

The composition and mechanical behavior of trabecular bone are important to understand for many biomedical applications. For example, in the case of a total hip replacement, most of the replaced bone is trabecular. The ideal hip replacement will closely match the properties of the

bone it replaces, as a mismatch in properties between an implant and surrounding bone is thought to be a source of implant failure. The mechanical behavior of trabecular bone is typical of a cellular material, as evident in the characteristic stress-strain plot of both materials. Additionally, modulus and strength of trabecular bone vary with density in a similar way to that of a foam [4]. Thus, it is reasonable to model trabecular bone using cellular material theory.

The stress strain curve for trabecular bone in compression shows the three distinct regimes of behavior typical of foam (Figure 4). In the first region, small strain and linear elasticity are observed. Stress results mainly from the bending of the cell walls. There may also be axial and membrane stress, but the stress contribution can be considered negligible, to a certain extent. It is important to note that in the case of stress-oriented bone, like the femoral head, the structure of the plate and rod like structures would be aligned in the direction of the largest principal stress, and loads applied in this direction may mainly extend or compress the cell walls, rather than bend, which would occur from a transverse load in this case. Plastic collapse marks the end of the linear elastic region, and is the point where rod and plate like walls would fail by elastic buckling (due to the high slenderness ratio). As strain progresses, compressive collapse is shown by the horizontal plateau until cell walls meet and stress rises steeply. This stage is known as densification [4].
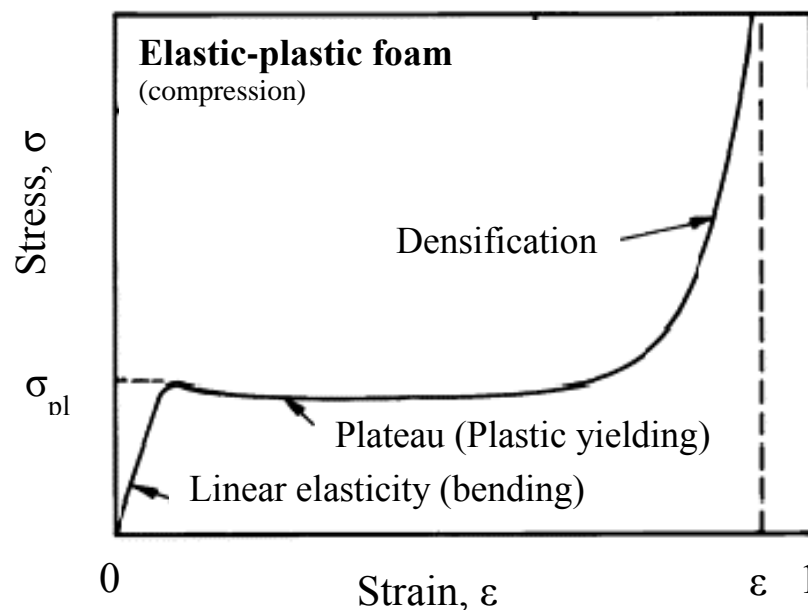
Figure 4: Characteristic compressive stress-strain curve of wet cancellous bone [4].

As can be expected, Young's modulus, compressive and tensile strength of cancellous bone are highly dependent on relative density. Figure 5 shows tensile strength for trabecular bone of unspecified orientation as a function of relative density. There is a large variance in the data from the studies shown because of trabecular bone anisotropy. Strength of bone also depends on strain rate, and the data displayed in the plots are from tests carried out at varying strain rates. There is also variance in the degree of dryness of the bone tested, another factor contributing to data variance [4].
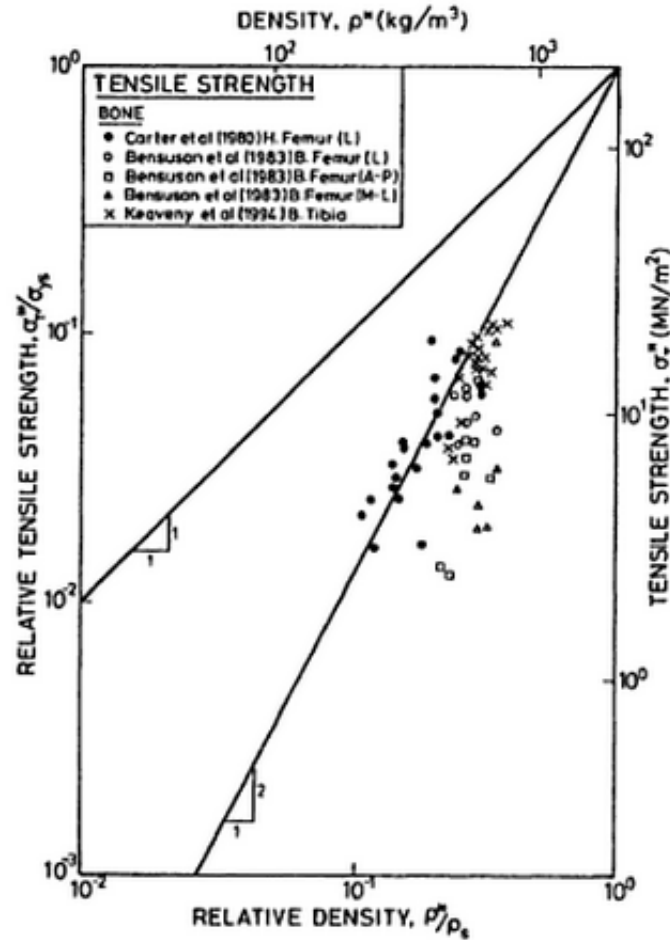
Figure 5: Tensile strength of trabecular bone as a function of relative density [4].

In summary, trabecular bone has a cellular structure, where the shape and density of the cells are biologically governed by the loads that bone must support. Cell walls of trabecular bone tend to align and thicken in the direction which will best support load, and the relative density of the cells depends on the load magnitude. In regions of low loading, trabecular bone tends to be

structured in a rod-like network of open cells, whereas in regions of high loading, the structure resembles perforated plates. Parallel plates tend to form along the lines of maximum principal stress. The mechanical behavior of trabecular bone is consistent with that expected of a cellular material, as shown in the stress-strain plot with three distinct regions of behavior. It is important to understand the structure and behaviour of trabecular bone in the field of biomechanics especially for the design of bone tissue replacements. With this understanding, a biomimetic implant can be designed, which closely matches the properties of the host bone tissue [4].

1.2 Tissue Engineering

1.2.1 Bone tissue scaffold

Bone tissue engineering is defined as any attempt to stimulate bone formation with an implant designed according to scientific and engineering principles [3]. Bone tissue implants are developed for the repair and replacement of damaged and diseased bone tissue by providing structural and cellular support for guided tissue formation. Traditionally, tissue repair was achieved by tissue grafting/transplantation, or synthetic material replacement. Bone grafting involves using bone from another source to stimulate bone formation at the site of a defect. The most preferable source of bone is from elsewhere in a patient's body; for example, from the pelvis (autologous graft). It is also possible to use bone from other humans (allogenic graft) or animals (xenogenic graft). Allografts generally undergo several treatments to reduce the opportunity for disease transmission and immunogenicity, such as extreme freezing and sterilization; however these procedures can reduce the osteoinductivity of the graft. Xenografts are used after demineralizing the bone matrix, so that the inorganic material is removed and just the organic collagen matrix is left behind. Demineralization results in a more biologically active graft than an undemineralized graft; however some mechanical properties are sacrificed [3].

Clinical outcomes of allografts and xenografts are variable [3]. For a bone graft to be successful, it must not interfere with normal physiological bone adaptation. This is why the autologous graft is most preferred, as it is not a foreign body. The autologous bone graft has been the golden standard for decades, and as such, it is used as a benchmark for alternative methods of grafting. It is recognized that there is a need for alternative graft options because of limited availability and increased surgical complexity of using autologous bone. Additionally, grafting necessitates a second surgical site [3].

The concept of tissue engineering using scaffold material emerged in the 1990s to address the limitations explained above [13]. The concept involves using degradable porous material scaffolds, sometimes integrated with biological factors, to regenerate tissue. The scaffold purpose is to provide temporary support as tissue regenerates and assumes primary function [13]. The scaffold architecture can be specifically tailored to provide a biomimetic mechanical environment while concurrently providing sufficient porosity for cell migration to achieve tissue regeneration [14].

Load bearing bone tissue scaffolds present certain design challenges that soft tissue scaffolds do not necessarily need to address. In the case of a permanent, non-degradable bone tissue scaffold, the implant must withstand relatively high physiological loading conditions as well as promote tissue regeneration at the periphery of the implant for fixation [15]. Approximately 1mm of bone ingrowth into the scaffold is required for biological fixation at the site. Technological advances in additive manufacturing have improved the feasibility of designing and fabricating scaffolds meeting these requirements. Combining computer aided design with additive manufacturing technology, which constructs structures in a layer by layer manner, allows for a fine control of scaffold design at both the macro- and micro-architectural level. This is demonstrated by Pasini et al. through the multi-scale and multi-objective design of a functionally graded cellular hip implant [16-21]. Pasini et al show that computational methods can be used to design a scaffold to meet specific mechanical and biological requirements, which are described in the following section.

1.2.2 Scaffold requirements

According to Hollister, there are four fundamental requirements that a bone tissue scaffold must satisfy, referred to as the 4F's: Form, Function, Formation, and Fixation. Form refers to scaffold shape completely filling a complex 3D anatomical defect. Function means supporting mechanical demands, i.e. normal physiological loading conditions. Formation refers to the enhancing tissue regeneration by providing a sufficient mass transport environment for new tissue growth. Finally, fixation means that the scaffold can be readily implanted and attached to a tissue at the defect site. These four requirements must be described in a quantitative manner so as to design a tissue scaffold [22].

With computer assisted design, the Form requirement can easily be fulfilled. For example, a scaffold can be specifically designed to fit an anatomical defect based on a patient CT

12

scan [15]. Factors affecting Fixation include scaffold microarchitecture (pore shape, size, interconnectivity), cellular interaction with the scaffold surface, and release of growth factors. The basic requirements of a tissue scaffold often present a design trade-off between Function and Formation: a denser, mechanically suitable scaffold versus a more porous scaffold which would provide better mass transport [13]. The requirements governing Formation are difficult to specify quantitatively. Bone regeneration is influenced by mass transport and delivery of biologics. Mass transport can be quantitatively expressed as permeability and diffusivity, which are controlled by the scaffold microarchitecture. Biologic delivery is dependent on the interaction between the scaffold and the local environment, scaffold degradation (if degradable), and mass transport [23].

It is therefore challenging to design a scaffold that addresses all four requirements for a number of reasons. Properties such as elasticity, permeability, and diffusion are related on a hierarchical scale (material and pore level) and require complex computational design and fabrication methods [23]. The exact target values for quantitative design requirements are often unknown, and in order to establish them, it must be possible to design and manufacture scaffolds with specified properties for testing. The factors affecting the 4F requirements are described in detail in the following sections.

Mechanical Properties

A bone implant must have sufficient mechanical properties to substitute for the loss of function of the replaced bone tissue [15, 24]. It is widely accepted that scaffolds should be designed to match healthy tissue stiffness and strength while providing a suitable network of pores to allow for cell migration and nutrient transport [25].

Over-designing for mechanical loading can result in a scaffold that is too stiff compared to the local tissue environment. In this case, a much stiffer scaffold can have adverse effects on local tissue, such as bone tissue resorption. Titanium and stainless steel are often used in orthopaedic implants because of their biocompatibility and superior mechanical properties compared to bone. However, a solid metal implant may absorb the forces that are required to stimulate bone remodeling. This phenomenon is known as stress shielding. The stress shielding effect can lead to bone resorption around the implant and prevent implant fixation [3]. Ideally, the mechanical properties would be similar to that of the local environment, so that scaffold failure would not occur, but structure stresses would be low enough to avoid tissue resorption [22].

13

Permeability/Diffusivity

A scaffold should provide an adequate environment for mass transportation of nutrients and metabolic waste [15, 24]. Mass transport can be quantitatively expressed as permeability and diffusivity. Permeability relates fluid velocity in a porous medium to the pressure gradient, and diffusivity relates ion concentration to chemical concentration gradients.

The permeability and diffusivity parameters of a scaffold should be targeted to align with the metabolic activity of the local tissue. For example, bone is highly vascularized and has relatively high metabolic activity. It is reported by Sander et al. that the permeability of trabecular bone is $0.003\text{-}11e^{-6}$ $m^4N^{-1}s^{-1}$, compared to articular cartilage which is $0.01\text{-}19.5e^{-15}$ $m^4N^{-1}s^{-1}$ [26]. The permeability of a scaffold will influence the oxygen diffusion to the local cells. The partial oxygen pressure (PO_2) is reported to affect the type of tissue formed from cell differentiation. For example, it was shown by Utting et al. that a PO_2 of 21% favours bone matrix production by osteoblasts rather than a low PO_2 of 2% [27] [22]. Therefore, an artificial scaffold should be designed with high permeability, similar to that of trabecular bone.

Osteoconduction/Osteoinduction

In certain instances, bone tissue scaffolds may be held in place by bone cement (PMMA for example), but in recent years, the design of cementless scaffolds has been given particular focus [28]. These implants are held in place permanently by bone tissue ingrowth. In addition to being biocompatible, a bone tissue scaffold requires optimal surface properties for the attachment, migration, proliferation and differentiation of bone cells [15]. Therefore important design considerations of a bone tissue scaffold are its osteoconductivity and osteoinductivity.

Osteoconductivity refers to how well bone cells can attach, proliferate and deposit bone on the scaffold. Osteoinductivity refers to the stimulation of osteoprogenitor cells to differentiate into osteoblasts, which begin new bone formation. Osteoinductivity can be achieved using growth factors that enhance bone healing [3]. Micro-pores increase the surface area of the scaffold and have been shown to trigger relevant cells that differentiate into osteoblasts. The micro-pores may be responsible for accelerating the process of dissolution/re-precipitation of calcium phosphates at the scaffold-bone interface [29]. In other words, the osteoinduction of the scaffold is increased as a result of increased surface area.

Tissue engineered implants can be comprised of a scaffold carrying biologically active factors, which may be a combination of cells and growth factors that stimulate host tissue growth

[3]. Cell-based bone tissue engineering is a technique that involves harvesting and expanding specific cell types in culture, known as bone marrow-derived stromal cells (BMSCs), and seeding the cells onto a scaffold. Most BMSCs successfully differentiate into cells of the osteogenic linage in vitro; however, it is found that in vivo differentiation is less predictable [3]. Growth factors are signaling molecules that influence cellular function, such as osteoinduction, by binding to specific receptors on the cell membrane. For example, bone morphogenetic proteins (BMPs) are growth factors found in extracellular bone matrix and can induce bone growth [3].

Microarchitecture

The need to match complex anatomic shapes and desired physical properties requires the separation of a scaffold into the microscopic (<1mm feature size) and macroscopic scales (>1mm). Scaffold microarchitecture refers to the microscopic design features that can be specifically tailored to achieve desired field properties throughout the scaffold. The division of feature sizes into two scales allows the utilization of areas of the design space which are not accessible with a solid material [15]. For example, the bounds on effective mechanical and mass transport properties are defined by properties of a completely solid material and no material at all. The range of possible effective properties fall within these bounds and can be achieved through the design of the microarchitecture. Tailoring the microarchitecture allows for the achievement of target properties such as elasticity, diffusion, and permeability, which meet the 4F requirements [30]. Some microarchitecture characteristics that are reported to influence tissue regeneration and vascularization include total porosity, pore size, pore interconnectivity, and pore geometry [25]. These characteristics are defined in detail below.

Porosity is crucial to facilitate bone growth. Additional porosity increases surface area and allows for mass transport of nutrients and metabolic waste [3]. Porosity is measured as the ratio of void space to total bulk volume of a scaffold. The surface of a bone tissue scaffold should be approximately 60-70% porous in order to effectively promote bone in growth. Inversely, the relative density of a scaffold is measured as the ratio of solid material to total bulk area. The optimal average size of a pore for bone tissue ingrowth in a scaffold material is in the range of 50-400 microns. Studies examining the effect of pore size found that both amount and rate of bone growth increase with decreased pore size, when comparing pores in the pore range

200-500 microns [31]. An interconnected porous architecture is necessary because it allows blood vessels and surrounding bone to enter the scaffold [3].

Many studies have shown that the rate of bone tissue growth by osteoblasts is influenced by scaffold geometry, implying that bone cells are able to sense their surroundings and react to local curvature, even if the curvature is much larger than themselves (Rumpler, 2008). Rumpler et al. examined new tissue growth on hyroxylapatite plates with a designed architecture, cultured in osteoblast-like cells. When comparing pores of triangular, square, and hexagonal geometries, tissue was found to be thickest in the corners of the triangular cells. Regardless of the original shape of the cell, tissue tended to round corners to form a circular central opening. Rumpler et al. concluded that the total amount of new tissue formed is highly dependent on the perimeter available within the cell: the shorter the perimeter, the more tissue formed at any point (Rumpler, 2008).

Similarly, Sikavitsas et al. conducted a study comparing the effect of pore geometry, and found that the least amount of tissue growth was shown in the corners of hexagonal shaped pores in a scaffold, whereas the highest amount of growth was found in the corners of triangles. Thus, the amount of initial tissue growth increases with increasing pore curvature. It is important to note, however, that the effect of pore shape on initial tissue growth does not hold true at later stages, once the pore shapes have all become circular (Sikavitsas, 2001). It was commented by Knychala et al. that it is important to find a balance between high curvature for initial tissue growth and porosity for permeability reasons. It may also be beneficial to design a balance between narrow aligned channels to achieve rapid tissue formation, and slightly bigger channels for the formation of osteons and vascularization [31].

A recent study by Van Bael et al. aimed to gain insight into the influence of scaffold pore shape, pore size and permeability on growth and differentiation of human periosteum-derived cell cultures (hPDC) [32]. The scaffolds were constructed out of Ti6Al4V in six distinct geometries: three different pore shapes (triangular, hexagonal, and rectangular) at two different pore sizes (500 and 1000 microns). They observed, similarly to Rumpler et al., that cell growth was governed by a circular growth pattern regardless of pore shape and size, eventually leading to pore occlusion. Qualitative examination of the six different scaffolds through SEM revealed that there was higher tissue growth on the periphery of the smaller (500 micron pore) scaffolds,

but after 14 days the 1000 micron pore scaffolds had higher living cell density. The pore shape caused higher distribution of cells in the corners of all pores. The group concluded that a graded scaffold is best for bone tissue regeneration, where the outside should be comprised of small pores for initial cell attachment, with large non-circular pores to avoid pore occlusion and allow for mass transport [32].

1.2.3 Design conflict: mechanical vs. mass transport function

Scaffold design is challenging because effective properties for mechanical support typically conflict with mass transport properties, which are essential for tissue regeneration. The increase in stiffness and strength of a scaffold comes at the expense of mass transport, and the opposite is also true (Figure 6).
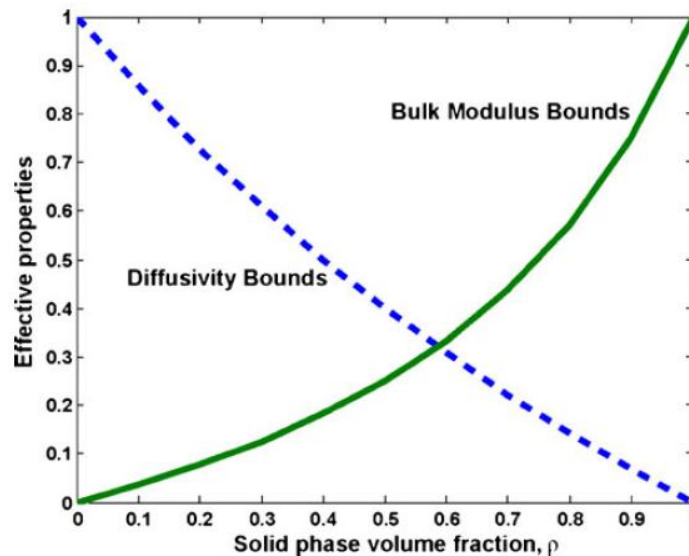
Figure 6: Normalized diffusivity and bulk modulus bounds for an isotropic two-phase material (e.g. solid-void) conflict as a function of volume fraction (relative density) [33]

Cellular material provides a unique advantage in addressing this trade-off because both macroscopic and microscopic features can be specifically tailored for mechanical and permeability properties using computational methods [13]. It is desirable to turn to optimization techniques to determine the material layout of a scaffold that can achieve these target effective properties [30]. In the past years, solid freeform fabrication techniques have increased in capability and are readily available for the production of scaffolds with highly controlled microarchitecture. In conjunction with computer assisted design, it is possible to manufacture a specifically tailored bone tissue scaffold [25].

1.3 Thesis Objective

The objective of this thesis is to illustrate that cellular material can be designed to address the multi-scale requirements of a bone tissue scaffold. In order to design a biomimetic bone tissue scaffold, the hierarchical structure of bone necessitates multi-scale design techniques. Using computational methods, both the scaffold geometry and its microarchitecture can be designed to achieve specific effective mechanical and mass transport properties. A porous scaffold can be manufactured using a biocompatible material (e.g. Ti-6Al-4V) by available additive manufacturing techniques, such as electron beam melting (EMB). EMB, and other additive manufacturing technologies, can create detailed metal constructs with extremely fine features on the micrometer scale. This thesis proposes a novel hierarchical topology optimization scheme as a computational method for the multi-scale design of bone tissue scaffold, and illustrates a 2D application.

The proposed procedure is applied to the design of an internal bone fracture fixation plate. Internal fracture fixation plate and screw systems are a method of treating fractured long bones. The purpose of the mechanism is to provide necessary stabilization and a critical amount of compressive stress at the bone fracture site to facilitate healing. Additionally, the plate must minimize devascularisation at the site, and allow early motion and partial loading to restore some load bearing capacity of the bone [34]. Compression also helps prevent transverse displacement of bone fragments and torque about the long axis of the bone [35]. The compression plate and screw components are typically made of solid, rigid, biocompatible materials such as stainless steel, cobalt chromium, titanium, and composites.

Ongoing concerns with fracture fixation plates are (1) excessive stiffness resulting in stress shielding, and (2) osteoporosis of underlying bone. The resulting decrease in bone mass and density increases the risk of re-fracture at the site [36]. One cause of osteoporosis beneath a fracture fixation plate is disruption of the periosteal capillary network at the fracture site. Areas of bone in contact with the plate receive insufficient blood supply and necrosis follows. Low contact surface plates and limited contact dynamic compression plates have previously been designed to reduce the disruption of blood flow [36]. Stress shielding results from the mismatch of mechanical properties between the bone and plate, resulting in bone resorption. Lower stiffness and functionally graded bone plates have been investigated to address this issue with varying success in results [37] [38].

It is hypothesized in this thesis that a hierarchically designed plate of cellular material can address both the stress shielding and osteoporosis problems with current fracture fixation plates. The porous nature of the cellular material reduces disruption of blood flow to the bone, while the mechanical properties are specifically tailored at the unit cell level to match that of the local tissue and reduce stress shielding. A hierarchical topology optimization approach will be used to design the plate at both the macro and micro scales; that is, at the material distribution of the implant and at the cellular material making it up. The design and optimization are performed in two dimensions, as the dominant forces acting on a fracture fixation plate are in-plane.

1.4 Thesis Organization

Chapter 2 of this thesis details the methods and theory involved in the design and analysis of bone tissue scaffold. The computational mechanics of cellular materials is discussed, followed by a description of topology optimization and hierarchical topology optimization theory. Previous literature on this topic is reviewed. Chapter 3 describes the proposed methodology for hierarchical design of bone tissue scaffold. A detailed flow chart illustrates the procedure. Design assumptions are discussed to define the scope and limitations of the proposed procedure.

Chapter 4 shows the application of the methodology to the design of a fracture fixation plate. Firstly, the optimal material distribution and geometry of the implant is determined. Secondly, each unit cell of the material is optimized based on bone tissue scaffold requirements described in Chapter 1. The result is a hierarchically optimized bone tissue scaffold, illustrating the novel design procedure proposed in this thesis. Finally, Chapter 5 discusses the relevance and validity of the design procedure and results, as well as proposes future extensions for this work.

Chapter 2: Methods and theory

The hierarchical structure of bone necessitates multi-scale design of a bone tissue scaffold. The hierarchical design of a cellular bone tissue implant is treated here as a material distribution problem at two geometric scales, as shown in Figure 7: (1) macro-architecture: topology of the implant, and (2) micro-architecture: topology of each unit cell. Firstly, the geometry of the implant is determined. The goal is to then realize this geometry using a cellular material with non-uniform unit cells, such that the implant can mimic the non-homogeneous material properties of bone. The implant geometry is mapped with unit cells which are specifically designed for the functional requirements at each location of the implant.
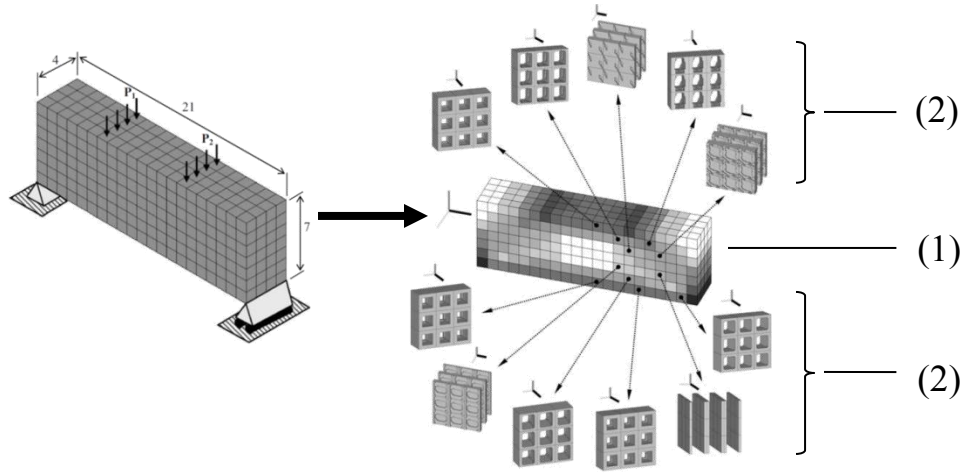
Figure 7: Hierarchical design of a structure using cellular material [39].

This chapter first discusses methods used to determine effective stiffness and permeability properties of cellular materials, as the design goal here is achieving a structure with specific effective properties. Next, topology optimization is discussed as a technique used for determining the optimal distribution of material to achieve a specific function. In general this involves finding an optimal material layout within a prescribed design space under defined constraints. In the proposed methodology, topology optimization is used at both the macro and micro scales to design a cellular structure guided by bone tissue scaffold requirements. The formulation of a multi-objective optimization problem to achieve conflicting stiffness and permeability properties is reviewed. Finally, an overview of existing hierarchical topology optimization methods is included in this chapter, as a reference for current state of the art in hierarchical structure design.

2.1 Computational mechanics for scaffold material

The macroscopic behaviour of a composite material is largely dependent upon its microstructure. However, the analysis of the structural mechanics of a cellular material is challenging due to large geometric heterogeneity at the microscopic level [40]. Extensive work on the characterization and structural analysis of lattice materials has been conducted by Pasini et al., and is used as a foundation for the techniques used in this thesis [41-49]. This section is focused on the computational methods used to determine effective (or equivalent) cellular material properties. Techniques to determine effective stiffness and permeability are discussed and a model of the mechanobiological behaviour of bone growth is reviewed.

2.1.1 Effective Stiffness

Analysing large cellular structures on a microstructural level is challenging because the highly complex geometry requires a large computational effort. Finite element analysis of microscopic behaviour is generally unfeasible, as it would be very computationally expensive to create, mesh, and analyse each strut of a discrete lattice [50]. As such, homogenization methods are developed to accurately approximate the behaviour and properties of a composite cellular structure based on the smallest repeating element of the structure: the unit cell, or the RVE (representative volume element).

Asymptotic homogenization is one among the several methods available in literature to determine an equivalent homogenous structure representing its detailed cellular counterpart [51]. Asymptotic homogenization is based on decoupling the analysis of a cellular material into analyses at the micro (local) level, and the macro (global) level. The method involves first analyzing one unit cell to determine its effective properties, by finding its unique behavioural response to a specified loading condition under periodic boundary conditions. To determine the effective stiffness matrix ($\boldsymbol{C}^H$) of a unit cell, a load is applied in each of the unique normal and shear directions, a process equivalent to imposing unit strains. The unit cell can then be treated as an equivalent homogeneous structure with the behavioural response equivalent to that of the detailed unit cell. Then, the entire macro structure can be mapped with equivalent homogeneous cells. This allows for a much simpler analysis of the structure at the global level.

The two explicit assumptions made in homogenization theory are: 1) fields vary on multiple spatial scales due to the existence of a microstructure, and 2) the microstructure is

spatially periodic [50]. Using the assumption of periodicity, the differential equations with rapidly oscillating coefficients that represent the microstructure are replaced with differential equations with slowly varying or constant coefficients, in such a way that the solutions for both sets of equations are approximately identical. Homogenization can be used for any periodic physical property, and is used to calculate effective stiffness in the proposed methodology [50]. The detailed derivation of the homogenization equations has been purposely included in Appendix A to avoid text flow disruption.

2.1.2 Effective permeability

Stokes flow homogenization

One approach to determining effective permeability of a cellular material is a homogenization technique based on the Stokes flow analysis of a unit cell. On the macroscopic scale, Darcy's law governs flow through a porous material. Darcy's law states that there is a proportional relationship between the instantaneous discharge rate through a porous medium, the fluid viscosity and the pressure drop over a given distance. At the microscopic scale, Stokes equations govern fluid flow through void areas of the unit cell. That is, the conservation of momentum is satisfied, acceleration of fluid is zero and there is a no slip condition at the fluid-solid interface. Sanchez-Palencia derived Darcy's law from Stokes equations using homogenization [52]. This works shows that an effective permeability tensor ($\mathbf{K}^H$) of a porous medium can be expressed as an ensemble average of fluid velocities in the unit cell. The ensemble average refers to an average of fluid velocities over specifically chosen states of applied pressure to fluid in a unit cell. Similarly to the homogenization process to determine effective stiffness, unit pressure gradients are applied to a unit cell to determine characteristic flow fields. The ensemble average of the characteristic flow fields gives the homogenized effective permeability tensor of a porous medium [53].

Monte Carlo simulation

A study by Sinh Trinh et al. shows that the effective diffusivity coefficient of a porous media can be computationally determined using Monte Carlo simulations [54]. The procedure involves finding effective diffusivity of a Brownian tracer in a unit cell using Monte Carlo simulations. With the unit cell topology defined a priori, particles are modelled to execute Brownian motion through the material. Einstein's explanation of Brownian motion describing the dynamics of a particle justifies the simulation of the particle using a 'random walk'. The

theory says that the particle, suspended in a fluid distributed throughout the pores of a medium, will move about as a result of collisions of surrounding particles. Effective diffusivity can then be determined using a probability density function based on the simulation of many particles. The function is governed by the equation for mean square displacement of a particle:

$$\langle x^2 \rangle = 2nDt \tag{1}$$

where D is the molecular diffusion coefficient in the fluid of the void space, n is the dimension, and t is time. Fick's law describes diffusion in a porous medium in terms of the effective diffusion coefficient D_e. Thus, the mean square displacement becomes:

$$\langle x_m^2 \rangle = 2nD_e t \tag{2}$$

where x_m is the displacement of the particle. To non-dimensionalize the expression for D_e, it is recognized that when porosity is equal to unity (no obstacles), the effective diffusion coefficient is equal to the molecular diffusion coefficient. The step-length l of particle "steps" is chosen such that the molecular diffusion coefficient from the simulation agrees with the given molecular diffusion coefficient. Dimensionless displacement ξ and time τ are then defined as follows:

$$\xi = \frac{x}{l}, \qquad \tau = \frac{2nDt}{l^2} \tag{3}$$

Finally, substituting the dimensionless equations into the governing mean squared displacement equation gives:

$$\langle \xi^2 \rangle = \frac{D_e}{D} \tau \tag{4}$$

The mean square displacement of the Brownian particle executing a random walk in porous media is now given by ξ. Monte Carlo simulations are used to obtain $\langle \xi^2 \rangle$ and then the diffusion coefficient ratio D_e/D can be determined. The simulation is conducted for 100 particles randomly walking for a given amount of time. As expressed in Equation [4], the slope of the line of dimensionless time versus mean squared displacement is the ratio of effective diffusion coefficient to the free molecular diffusion coefficient. It was determined that in structured, isotropic media, effective diffusivities can be accurately characterized in this manner.

Sinh Trinh et al. compared effective diffusivity calculated for 2D porous media to experimental and theoretical data. When geometry and dimension of obstacles are consistent with those used in experiment, Monte Carlo simulations agree with experimental data. Figure 8 shows that the Monte Carlo simulations yield slightly lower effective diffusivities than

theoretical predictions by Maxwell and Weissberg, and postulate that differences arise from variance in geometries of media used to obtain results. The results in Figure 8 show that a "percolation threshold" exists in the data, which is the porosity at which a diffusing molecule can be trapped in an isolated pore, within the unit cell. At the percolation threshold, effective diffusivity as calculated in the Monte Carlo simulation vanishes. It is observed that for isotropic systems above a "percolation threshold", effective diffusivity is affected solely by porosity.
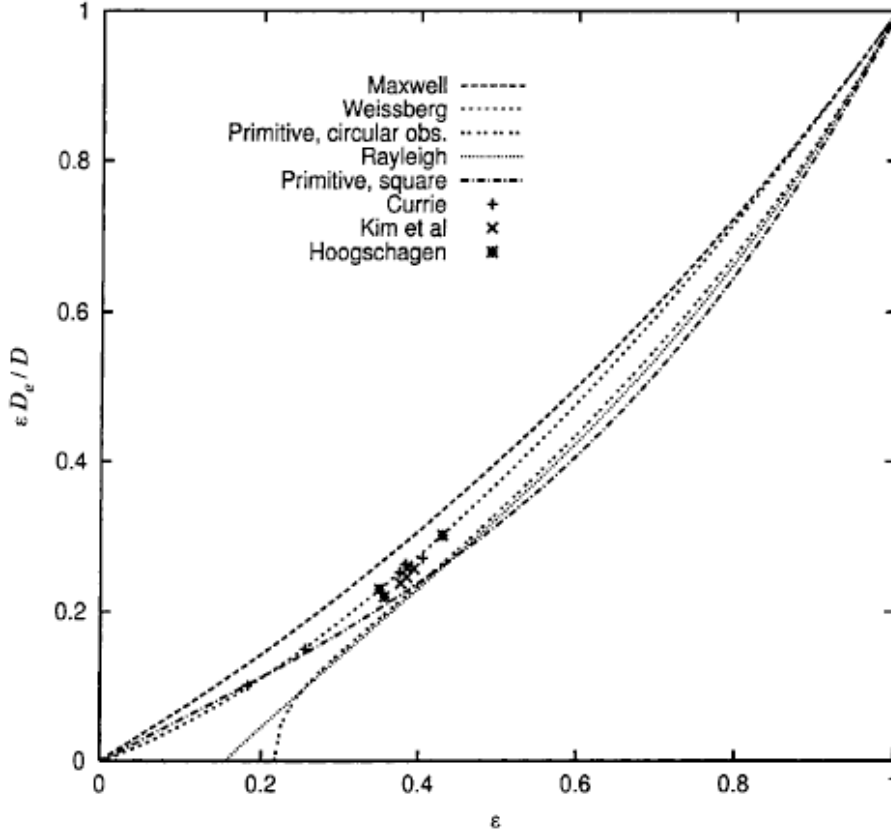
Figure 8: Effective diffusivities as a function of porosity ε obtained by experimental and theoretical methods and Monte Carlo simulations of flow in 2D porous media [54].

Weissberg's approximation

Weissberg's formula is an approximation that was originally derived to determine the effective diffusion coefficient through a bed of randomly overlapping spheres of uniform or non-uniform shape, and is solely a function of porosity, ε [55]:

$$\frac{D_e}{D} = \frac{\varepsilon}{[1 - \frac{1}{2} ln\,\varepsilon]} \qquad [5]$$

It is valid to use Weissberg's formula to approximate effective diffusivity in 2D porous media if the following assumptions can be made: (1) the media is isotropic and (2) the media porosity is above the percolation threshold. Because of good agreement of simulation results to the theoretical predictions in the range of 60-80% porosity shown in Figure 8 (above the percolation threshold and in the required bone ingrowth range), it is assumed that theoretical predictions can be used as an estimate of effective diffusivity. If the unit cells of a designed scaffold are constrained to be isotropic then assumption (1) will hold. As described in section 2.3.1, the desired outcome of this research is to optimize an overall anisotropic cellular medium with isotropic unit cells. Therefore, the Weissberg approximation will be used in the proposed optimization procedure to calculate unit cell diffusivity.

2.1.3 Mechanobiological Model

As an additional parameter for describing scaffold properties, a mechanobiological model can be used to characterize tissue growth. Chen et al. studied the effect of unit cell topology on the differentiation of stem cells into various tissue types in a scaffold [12]. It was found that scaffold microarchitecture is an influential factor in the direction of tissue differentiation because it directly affects mechanical stimulus experienced by surrounding tissue. Based on the mechanobiological model described by Prendergast [56], it is assumed that mechanical stimulus S in the unit cell is regulated by octahedral shear strain τ and fluidic velocity v:

$$S = \frac{\tau}{a} + \frac{v}{b} \tag{6}$$

Variables a and b are empirical constants [56]. The value of S can predict the differentiation of stem cells within the unit cell into various phenotypes using the following criteria based on experiment:

$$0.01 < S < 0.53 \quad \text{Mature bone}$$
$$0.53 < S < 0.1 \quad \text{Immature bone}$$
$$1 < S < 3 \quad \text{Cartilage}$$
$$3 < S \quad \text{Fibrous tissue}$$

If S is lower than 0.01, bone resorption occurs according to this model. Varying topologies to either favour stiffness or permeability properties show a range of tissue regeneration response, supporting the theory that microarchitecture has a strong influence on neo-tissue formation.

It is noted by Chen et al. in further work that cellular materials for tissue regeneration should possess cell-favourable microfluidic properties in terms of flow velocity and wall shear stress (WSS) [28] . The magnitude of wall shear stress can be calculated as a function of dynamic viscosity. Chen et al. used computational fluid dynamics analysis to obtain WSS, and their results support the hypothesis that unit cell designs which elicit uniform WSS can enable cells to differentiate and grow into tissue in a desirable uniform fashion.

2.2 Inverse Homogenization

As discussed in section 2.1.1, homogenization theory is used to calculate the effective properties of a bulk material based on knowledge of the topology of a repeating unit cell. Recalling the goal of designing a bone tissue scaffold with specific effective properties, it is therefore necessary to solve an *inverse homogenization* problem [53]. Inverse topology optimization was originally introduced by Ole Sigmund who formulated the problem as a minimization of the difference between homogenized material properties and target material properties of a unit cell. The goal is to seek a microstructural configuration that attains desired effective material properties [57]. This procedure is described below.

At the microscopic level, the problem becomes determining material distribution within the design domain of the unit cell. The unit cell is discretized into uniform mesh elements, each of which possesses a relative density: a fraction indicating how much solid material phase is present in that element. A relative density of 1 indicates completely solid material, and a relative density of 0 indicates a void element where no material is present. The connection of solid elements defines the topology of the unit cell and consequently the effective properties. Relative densities of the elements of the unit cell are typically the design variables when using topology optimization to solve the inverse homogenization problem.

There are two common approaches to defining objective functions for finite element based inverse homogenization. The first is minimizing or maximizing critical components of a homogenized tensor. This is formulated for the stiffness tensor as minimizing these parameters (or their reciprocal). For example maximizing bulk modulus can be formulated as:

$$\min_{\rho} f(\rho) = \left(\frac{1}{9} \sum_{i,j=1}^{3} C_{iijj}^{H}(\rho) \right)^{-1} \qquad [7]$$

where ρ is relative density and C_{iijj}^H is the homogenized stiffness tensor. The second approach is using the least squares formulation, where the square of the difference between homogenized tensor and target tensor is minimized. It is mathematically formulated in the following way:

$$\min_{\rho} f(\rho) = \sum_{i,j,k,l=1}^{3} w_{ijkl}(C_{ijkl}^* - C_{ijkl}^H)^2 \qquad [8]$$

where w_{ijkl} is a weighting factor to vary roles of different stiffness components and C_{ijkl}^* is a target stiffness tensor.

The method of inverse homogenization is well suited for our application of specifically designing a bone tissue scaffold. The goal in such design problems is typically to match the stiffness of the surrounding tissue while maximizing permeability. The hierarchical design of the bone tissue scaffold is addressed by using multi-functional inverse homogenization at both the macro and micro scales, with topology optimization used to solve the inverse homogenization problem.

2.3 Topology optimization for bone tissue scaffold

Bendsøe and Sigmund describe in detail the theoretical basis for topology optimization in their book "Topology Optimization: Theory, Methods, and Applications" [58]. The following section and many published works in this area are based on their derivative of the topology optimization approach to inverse homogenization. Topology optimization is the basis of the proposed technique for designing a bone tissue scaffold with desired stiffness and permeability.

2.3.1 Definition and derivation

A structural design problem can be broken into categories of sizing, shape, or topology optimization, each addressing different aspects of the design as depicted in Figure 9. An example of a sizing problem is finding the optimal thickness distribution of a plate, with the goal of minimizing or maximizing a certain physical quantity subject to equilibrium and other constraints on the state. For example, the optimal material distribution for the plate may minimize mean compliance, subject to a deflection state constraint, where the design variable is plate thickness. The characteristic feature of a sizing problem is that the design model domain and state variables are known and fixed *a priori*. In contrast, the goal of a shape optimization problem would be to find the optimum shape of this domain, where the domain boundary becomes the design variable. Shape optimization problems are restricted in that the topology (the

location and formation of holes) does not change from the initial design to the final design. In many cases, however, the introduction and removal of holes without violating design constraints has an advantage compared to shape optimization since it can lead to a better optimal layout [59].
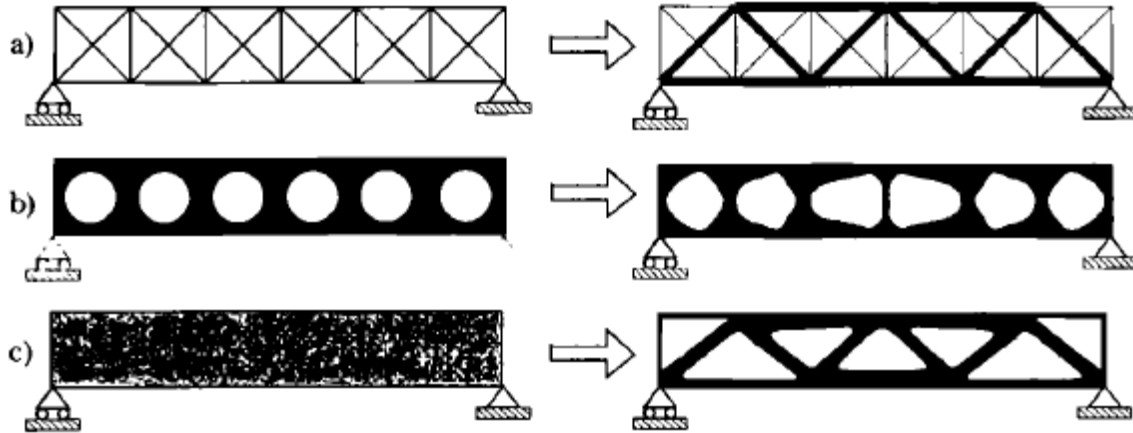

Figure 9: The three categories of structural optimization: a) Sizing of a truss structure, b) shape, and c) topology. Initial designs are shown on the left and final designs are shown on the right [58].

Topology optimization refers to the determination of the connectivity of the design domain, through features such as number, location, and shape of holes in a structure. The goal of topology optimization is to determine the optimal placement of an isotropic material in a given design space. It should be noted that although the base material is isotropic, the desired outcome of this research is to optimize an overall anisotropic cellular material. In a topology optimization problem, the known quantities would include applied loads, boundary conditions, desired volume of the structure (or desired compliance), and any specific structural design restrictions such as areas of solid material or holes. The connectivity and shape of the structure are unknown. A set of distributed functions defined on the fixed design domain are used to represent the topology, size, and shape of the structure.

A general shape optimization problem formulated as a material distribution problem is a starting point for topology optimization. A widely applicable material layout problem consists of designing for minimum compliance with material constraints. The problem formulation is described below.

A solid body occupying a domain Ω_{mat} is part of a larger reference domain Ω in R^2 or R^3. The problem of finding an optimal design in this context is finding the optimal choice of the stiffness tensor $E_{ijkl}(x)$ of the solid body, which is variable over the domain. A typical approach to finding the minimum compliance problem is to discretize the problem using finite elements. A problem that arises automatic generation of holes in a design space is that re-meshing capabilities must be embedded to account for the iterative changes in topology (i.e. the introduction of a hole). To address this issue, a fixed mesh can be used where void elements can be assigned very low stiffness properties, so that re-meshing is avoided and holes can be introduced [59]. Both the displacement and stiffness fields are discretized using identical prescribed mesh. The minimization problem becomes:

$$\min_{u,E_e} \quad \boldsymbol{f}^T \boldsymbol{u} \qquad\qquad [9]$$

$$s.t. \quad \boldsymbol{K}(E_e)\boldsymbol{u} = \boldsymbol{f}$$

$$E_e \in E_{ad}$$

Where $\boldsymbol{f}$ and $\boldsymbol{u}$ are the load and displacement vectors respectively, the stiffness matrix $\boldsymbol{K}$ is a function of E_e in an element e, and E_{ad} is the set of admissible stiffness tensors for the given problem. The stiffness matrix $\boldsymbol{K}$ can be written as a sum of stiffness of each element in the form:

$$\boldsymbol{K} = \sum_{e=1}^{N} \boldsymbol{K}_e(E_e) \qquad\qquad [10]$$

where element e is numbered as $e = 1, \dots, N$ and $\boldsymbol{K}_e$ is the global level element stiffness matrix.

In a discretized design space, the topology of a structure can be visually represented as a black and white rendering of the pixels (or voxels, in 3D). In these terms, the design problem involves finding the optimal subset Ω_{mat} of material pixels. The set of admissible stiffness tensors consists of those tensors for which:

$$E_{ijkl} = 1_{\Omega^{mat}} E_{ijkl}^0, \quad 1_{\Omega^{mat}} = \begin{cases} 1 \; if \; x \in \Omega^{mat} \\ 0 \; if \; x \in \Omega \backslash \Omega^{mat} \end{cases} \qquad\qquad [11]$$

$$\int_{\Omega} 1_{\Omega^{mat}} d\Omega = Vol(\Omega^{mat}) \leq V \qquad\qquad [12]$$

The inequality expression [12] imposes a limit on the volume fraction V of material that can be used in the design, resulting in a minimum compliance design for a fixed volume. The stiffness tensor E_{ijkl}^0 is for a given isotropic material, which varies with point x over the domain. Solving

29

this problem is most commonly achieved by replacing the integer variables $(1_{\Omega^{mat}})$ with continuous variables, and applying a penalty that will direct the solution to have a binary 0-1, void-solid material distribution. With a fixed domain, the problem becomes a sizing problem by modifying the stiffness matrix to depend on a continuous function representing the density of the material. The function representing density is the design variable.

2.3.2 Solid Isotropic Material with Penalization method

The introduction of a penalty allows for the design of a structure with regions of either solid material or void space, as opposed to an intermediate value. A popular and efficient penalization method is called "Solid Isotropic Material with Penalization", i.e. SIMP. Using the SIMP method, the sizing problem would be reformulated with penalization factor p as:

$$E_{ijkl} = \rho(x)^p E^0_{ijkl}, \quad p > 1 \tag{13}$$

$$\int_{\Omega} \rho(x)d\Omega \leq V; \quad 0 \leq \rho(x) \leq 1, \quad x \in \Omega \tag{14}$$

The continuous density function $\rho(x)$ is the design variable and E^0_{ijkl} is the isotropic base material stiffness. The stiffness tensor E_{ijkl} interpolates between 0 (void space) and E^0_{ijkl}. The penalization method is commonly used in structural optimization where intermediate values of material density do not have physical meaning, and a completely solid-void design is desired. With the exponent on the density function $p > 1$, values of density that are in the intermediate range are penalized because a smaller stiffness is obtained for a given material volume. Thus, it becomes uneconomical to use intermediate density values[60].
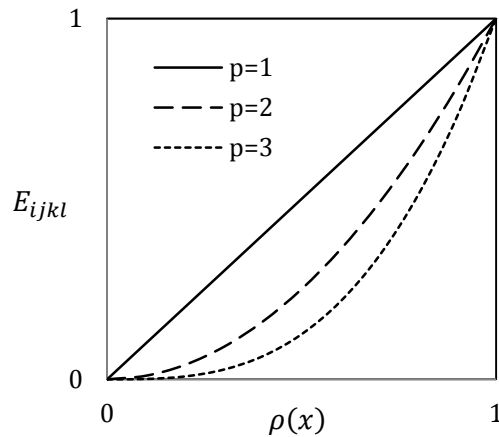

Figure 10: Effect of penalty factor p in SIMP method.

Often, $p \geq 3$ is used to obtain designs that are 0-1. Rietz shows that for a large enough p, there is a global optimum solution in 0-1 form, as long as the volume constraint is compatible [61]. Too severely penalizing the function, however, can result in a design that is a local minimum which is overly sensitive to the choice of the initial design. That is, the design jumps too quickly to a 0-1 design. The choice of p is dependent on the design problem. A method of slowly raising the power p through the computations is suggested, until the final design is reached [60].

The physical interpretation of SIMP-model can be visualized using a composite or cellular material. If each pixel of a mesh is regarded as one unit cell, a design which has some grey regions can be achieved by designing the topology of each unit cell to match the required relative density.

2.3.3 Stress constraint

It is common that topology optimization will lead to designs that have high stress concentrations or even stress singularities [62]. Often, shape optimization and design adjustments are conducted a posteriori to fulfil stress constraints. It is shown in literature that stress constraints can also be included in topology optimization to circumvent or simplify *a posteriori* the material design. In 2013, Holmberg et al show that by including a stress inequality constraint in the topology optimization statement, designs can be achieved to avoid stress concentrations [62]. Avoiding stress concentrations is essential to the longevity of a bone tissue scaffold, as plastic deformation could lead to fatigue and failure. In topology optimization where there may be intermediate values of local relative density, stress constraints cannot be defined a priori because local material properties change as a function of relative density. Using the SIMP model, the stress constraint can be formulated as:

$$\sigma_{VM} < \rho^p \sigma_l$$

where σ_{VM} is the von Mises equivalent stress, ρ is local relative density, p is the penalty factor (see section 2.3.2) and σ_l is local stress [58]. This formulation has not been implted in the current thesis and will be part of future study.

2.3.4 Optimization methods

Common algorithms specific to topology optimization include the Optimality Criteria (OC) method, the Method of Moving Asymptotes (MMA), and the Level Set Method (LSM) [57]. Evolutionary Structural Optimization (ESO) and Genetic Algorithms (GA) are alternatives

to the gradient based methods, but are currently not as commonly used in topology optimization procedures for multi-functional bone tissue scaffolds. Two gradient based optimization procedures are described below that are compatible with topology optimization: OC and MMA.

Optimality Criteria Method

In topology optimization, an iterative method is used to update relative density of each element. The relative densities are updated independently from the other elements and with respect to conditions of optimality, based on a previously computed design. The conditions of optimality for minimum compliance design of a structure using the SIMP interpolation scheme is described in this section.

The derivation of the conditions of optimality begins with an expression of energy in the bilinear form. Energy as an expression of the internal virtual work of an elastic body at the equilibrium u and for an arbitrary virtual displacement v is given by.

$$a(u, v) = \int_{\Omega} E_{ijkl}(x)\varepsilon_{ij}(u)\varepsilon_{kl}(v)d\Omega \qquad [15]$$

The minimum compliance problem with SIMP is formulated in weak form as:

$$\min_{u \in \boldsymbol{U}, \rho} l(u) \qquad [16]$$

$$s.t. \quad a_E(u, v) = l(v), \quad for\ all\ v \in U$$

$$E_{ijkl} = \rho(x)^p E_{ijkl}^0$$

$$\int_{\Omega} \rho(x)d\Omega \leq V; \quad 0 < \rho_{min} \leq \rho(x) \leq 1$$

Strain $\varepsilon_{ij}(u)$ and load $l(u)$ in linear form, respectively are:

$$\varepsilon_{ij}(u) = \frac{1}{2}\left(\frac{\partial u_i}{\partial x_j} + \frac{\partial u_j}{\partial x_i}\right) \qquad [17]$$

$$l(u) = \int_{\Omega} fud\Omega + \int_{\Gamma_T} tuds \qquad [18]$$

The load $l(u)$ is the work done by body forces f and traction t at the boundary. The variable f describes the body forces, and t is the boundary tractions on the traction part Γ_T of the boundary $d\Omega$. U is the space of admissible displacement fields and the subscript E on the energy equation indicates that it is dependent on the design variables. Relative density ρ must be greater than zero to avoid singularities in the equilibrium problem. It is sufficient to set $\rho_{min} = 10^{-3}$.

Reformulating the problem in Lagrangian form allows the conditions for optimality of ρ to be derived from the stationary conditions of the Langrange function. Using Lagrange multipliers Λ, $\lambda^-(x)$, and $\lambda^+(x)$ for the constraints of the minimum compliance problem, the Lagrangian function is written as follows:

$$L = l(u) - \{a_E(u, \bar{u}) - l(\bar{u})\} \tag{19}$$

$$+ \Lambda(\int_\Omega \rho(x)d\Omega - V) + \int_\Omega \lambda^+(x)(\rho(x) - 1)d\Omega$$

$$+ \int_\Omega \lambda^-(x)(\rho_{min} - \rho(x))d\Omega$$

For the equilibrium constraint, $\bar{u}$ is the Lagrangian multiplier. Assuming that $\rho \geq \rho_{max} > 0$, the optimality condition for variations of the displacement field u gives $\bar{u} = u$. To determine the optimality conditions for ρ, the derivative of the equation is taken and set to zero ($\nabla L = 0$):

$$\frac{\partial E_{ijkl}}{\partial \rho} \varepsilon_{ij}(u)\varepsilon_{kl}(u) = \Lambda + \lambda^+ + \lambda^- \tag{20}$$

The detailed calculation for the derivative of E_{ijkl} with respect to ρ is shown in Appendix C. The derivatives for each point are localized, but have influence from the surrounding elements through the displacement u. Both sides of Equation [20] have an integral over Ω which can be dropped. By inspection, the inequality constraints with multipliers λ^+ and λ^- are not active for intermediate values of ρ. That is, when $\rho_{min} < \rho < 1$, the optimality condition is:

$$p\rho(x)^{p-1}E^0_{ijkl}\varepsilon_{ij}(u)\varepsilon_{kl}(u) = \Lambda \tag{21}$$

This shows that the term on the left side of the equation, similar to the strain energy density, is constant and equal to Λ, the volume constrain multiplier, for intermediate densities. For an iterative scheme, the design variable ρ can be updated based on these optimality criteria to achieve a stationary Lagrangian system. Such an update scheme can be written as follows:

$$\rho_{n+1} = \begin{cases} max\{(1 - \varsigma)\, \rho_n, \rho_{min}\} & if\ \rho_n B_n^\eta \leq max\{(1 - \varsigma)\, \rho_n, \rho_{min}\} \\ min\{(1 + \varsigma)\, \rho_n, 1\} & if\ min\{(1 + \varsigma)\, \rho_n, 1\} \leq \rho_n B_n^\eta \\ \rho_n B_n^\eta & otherwise \end{cases} \tag{22}$$

The subscript of ρ_n is the value of density at iteration n, and B_n represents the optimality expression:

$$B_n = \Lambda_n^{-1}p\rho(x)^{p-1}E^0_{ijkl}\varepsilon_{ij}(u_n)\varepsilon_{kl}(u_n) \tag{23}$$

33

Here, u_n is the displacement field at iteration n. A local optimum is reached when $B_n = 1$ for intermediate densities. The update scheme can be interpreted as adding material to areas which have high strain energy (when $B_n > 1$) and removing material when strain energy is low. Otherwise, B_n is close to unity, and the optimality condition is satisfied for that design variable. It is shown that the update scheme accounts for the upper and lower bounds on allowable relative density (ρ_{min} and 1). There are two additional parameters in the update scheme: ς and η. The variable ς is a "move limit" which enforces a control on the amount that a design variable can change in one iteration. The tuning parameter η is chosen by experiment to obtain a stable and efficient convergence scheme based on the specific problem. The typical values used for η and ς respectively are 0.5 and 0.2.

The steps of topology optimization with the Optimality Criteria method can be summarized as follows:

1. Define the reference domain, and specify the areas which will be subject to optimization.
2. Create a finite element mesh of the domain for both the displacements and design variables (preferably the same size mesh).
3. Define initial distribution of material. This may be a homogeneous distribution. Begin the iterative process:
4. Apply load and boundary conditions, and calculate resulting strains by finite element analysis.
5. Compute the compliance of the design.
6. Check for design convergence – if the change between this structure and the previous is very small, stop the iteration. Otherwise, update the design variable based on the optimality criteria. Repeat the iterative process.

The optimality criteria (OC) method is effective for large scale topology optimization. However, the algorithm is not suitable for certain structural optimization problems. For example, multiple objectives and constraints, and constraints of geometric nature, may require a more costly, but more robust mathematical programming method. The method of moving asymptotes is a versatile algorithm, well suited to address the limitations of the OC method.

Method of Moving Asymptotes

The method of moving asymptotes (MMA) is a mathematical programing method, similar to Sequential Linear Programming and Sequential Quadratic Programming, which is well suited for topology optimization [58]. These methods solve smooth, non-linear optimization problems by using a sequence of subproblems which are simpler approximations. MMA uses separable and convex subproblems, which are chosen based on the sensitivity of a given design point and knowledge of previous iterations. Subproblems can be solved each iteration using algorithms such as the dual method, or the interior point algorithm. Optimization with MMA can be summarized in the following steps:

1. Choose a starting point $x^{(0)}$ and let iteration index $k=0$.
2. Calculate the behaviour constraints $f_i(x^{(k)})$ and gradients $\nabla f_i(x^{(k)})$ for given iteration point $x^{(k)}$ for $i=0,1,...,m$
3. Generate subproblem $P^{(k)}$ by replacing the implicit functions f_i by approximating explicit functions $f_i^{(k)}$ based on calculations from step 2.
4. Solve the subproblems and let the optimal solution of this subproblem be the next iteration point $x^{(k+1)}$. Let $k=k+1$ and go back to step 2. The process ends when user specified convergence criteria are met.

As shown in Equation [24] below, the approximations $f_i^{(k)}$ in step 3 are found by a linearization of f_i in variables $1/(U_i - x_i)$ and $1/(x_i - L_i)$ which are dependent on the signs of the derivatives f_i at $x^{(k)}$. The parameters U_i and L_i are "moving asymptotes" and change between iterations. The approximation is formulated as:

$$f_i(x^{(k)}) \approx f(x^0) + \sum_{i=1}^{n} \left(\frac{r_i}{U_i - x_i} + \frac{s_i}{x_i - L_i} \right) \tag{24}$$

The parameters r_i and s_i are chosen based on the following criteria:

$$if \; \frac{\partial f}{\partial x_i}(x^0) > 0 \quad then \quad r_i = (U_i - x_i^0)^2 \frac{\partial f}{\partial x_i}(x^0) \quad and \quad s_i = 0$$

$$if \; \frac{\partial f}{\partial x_i}(x^0) < 0 \quad then \quad r_i = 0 \quad and \quad s_i = -(x_i^0 - L_i)^2 \frac{\partial f}{\partial x_i}(x^0)$$

The separable property of the approximation subproblems means that the design variables are not coupled by the optimality conditions of the subproblems, and subproblems have a unique solution. The convexity property of the subproblems is what allows dual methods or primal-dual

methods to be used for solving. The combination of these properties results in a computationally efficient method for topology optimization [63].

This method may be slower than OC, but the MMA offers an advantage over OC because geometry considerations and situations with limited knowledge of the physical space can be accommodated, and the MMA can efficiently handle a large number of design variables. The method can also handle complex min-max functions. The method of moving asymptotes has one main disadvantage: convergence cannot be guaranteed [63]. A common experience with MMA is that if it converges, a solution is found quickly with steadily improving designs, but often the solution will diverge.

Numerical instabilities in topology optimization

Topology optimization approaches often suffer from a variety of numerical instability problems, such as checkerboard patterns, mesh dependence, and computational inefficiency. Checkerboard patterns refer to the case where solid and void elements appear in alternating fashion, only connected by a corner, and create artificially high stiffness regions. To avoid this problem, higher order mesh elements can be used. Techniques such as local gradient constraints, filtering, and various material interpolation schemes such as SIMP are also used to eliminate the presence of checkerboard regions [57].

Mesh dependency is a numerical instability illustrated in Figure 11, which shows that increased mesh refinement results in a larger number of holes appearing in the optimal topology.
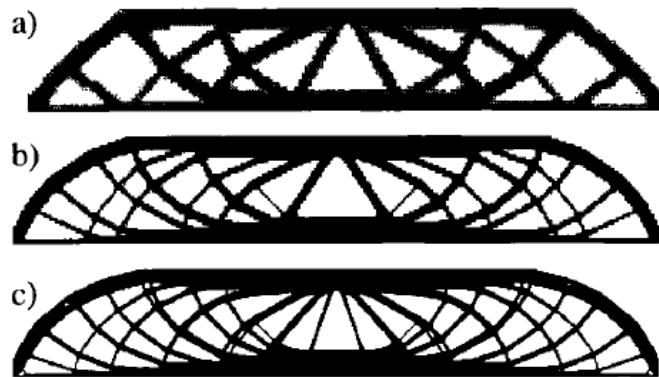

Figure 11: Dependence of optimal topology on mesh refinement. Solution is shown with a mesh of a) 2700 b) 2800 and c) 17200 elements [58].

Ideally, mesh refinement would result in a better modelling of boundaries of the same optimal topology. In the case shown in Figure 11, there is a non-existence of numerical solutions.

One way to efficiently achieve mesh independent designs is to reduce the design space of admissible design vectors with a global or local restriction on the variation of density. This can be achieved by either adding constraints to the optimization problem, reducing the parameter space directly, or applying filters in the optimization method. Convergence of finite element approximations can be found with the addition of one of these solutions [58].

One highly efficient filter to ensure mesh-independency is to modify design sensitivity in such a way that the sensitivity of a specific element is based on a weighted average of the neighboring element sensitivities in a defined fixed range. This is a heuristic method of filtering but it is computationally efficient and simple to implement. It is reported that results are very similar to those obtained by a local gradient constraint to achieve the same effect [58].

A minimum length scale constraint can also be applied so that there are no features on a similar length scale of a mesh element [53]. This helps to address manufacturing issues arising from small feature sizes, and is a method to avoid the ill-posed nature of topology optimization. The design space is thus restricted but it ensures that checkerboard free solutions can be found with mesh independence.

2.4 Multi-objective optimization

In multi-objective optimization, a *set* of optimal solutions is sought. This optimal set is called the Pareto front. Pareto optimal solutions means that X* is an optimal solution if there exists no feasible solution X which can decrease some objective without causing at least one other objective function to increase. Many methods can be used to obtain Pareto optimal solutions, the easiest of which to implement is the weighted sum method. As described in the Chapter 1, the design of a bone tissue scaffold presents a multi-objective design conflict in the requirement for maximized stiffness and permeability. Multi-objective optimization of lattice materials is illustrated by Faragelli et al. [64], and by Khanoki et al [19, 20] specifically to address bone scaffold requirements.

2.4.1 Weighted sum method

A multi-objective function can be formulated as a weighted sum of more than one (possibly conflicting) objective functions, each assigned a weighting a priori, where the total of the weights adds to 1. This method formulates a multi-objective problem as a single objective function. It should be noted that this method is not reliable for non-convex problems [65]. Chen

and Wu implement this method to address conflicting design requirements of minimum compliance and maximum eigenvalue [65].

While designing for maximum effective stiffness or maximum fluid permeability has been successfully attempted, the multi-objective problem of designing for both is more difficult [53]. In work by Guest et al. this multi-objective goal is formulated as a weighted sum. Three dimensional porous materials are simultaneously optimized for stiffness and fluid permeability while achieving target elastic and flow symmetries. The problem is formulated as an inverse homogenization problem, with relative density as the design variable. The objective function is a maximization of summed terms (effective stiffness and permeability) and an error function to enforce symmetries on both elastic properties and fluid flow. It is assumed that fluid velocities are uncoupled from matrix deformation, and homogenization of Stokes flow is used to calculate effective permeability. The MMA is used to solve the optimization problem with the SIMP penalty function. Solutions to this multi-objective design problem show that a range of materials can be designed within the design parameters by varying the weights of each objective in the objective function.

2.4.2 Theoretical bounds

A strategy used in multi-objective optimization is determining cross-property bounds between conflicting requirements a priori, to be used as a reference that can restrict the design space. Theoretical bounds on various conflicting properties can be calculated, and used in topology optimization to design cellular materials that extend the cross-property design space.

Effective bulk modulus and isotropic diffusivity cross property bounds are defined by Hashin and Shtrikman (among others), based on a given material volume fraction [33]. Hashin and Shtrikman derived these well-known bounds using variational principles. The upper bounds of these properties are theoretically defined as:

$$B_{max}^{iso} = \frac{(3/4)\rho BG}{(1-\rho)B + (3/4)G} \qquad [25]$$

$$D_{max}^{iso} = \frac{2(1-\rho)D}{2+\rho} \qquad [26]$$

where ρ is relative density, B and G are bulk and shear moduli of the solid phase, and D is the free isotropic diffusion coefficient of a solute in the fluid phase [33]. Kang et al. use these cross property bounds as design targets for their topology optimization procedure.

In other work, Challis et al. perform topology optimization of two phase periodic multi-functional composites in three dimensions using the level set method and cross property bounds [66]. The material studied has two phases: one stiff and insulating, and the other conductive and mechanically compliant. Cross property bounds were calculated and used here to demonstrate near-optimality of optimization microstructures.

Further work by Challis et al. computes Pareto fronts to estimate upper bounds of bulk modulus and permeability for cross-property space for periodic porous materials for a range of porosities. The Hashin-Shtrikman bounds on effective magnetic permeability of composites are analogous to electrical conductivity, thermal conductivity, and diffusion coefficient. This paper shows that the bulk modulus and fluid permeability cross property space is not convex and therefore the full Pareto front cannot be realized [67]. A study by Hollister et al. compared their optimal designs to bounds on effective elastic modulus for isotropic and cubic symmetry cases [30]. It was shown that a significant portion of theoretical bounds for effective stiffness can be achieved with topology optimization.

2.5 Target matching topology optimization

In target matching topology optimization, the goal is to design a material with predefined structural properties. This can be expressed using the least squares formulation, where the square of the difference between a homogenized property and target property is minimized. Using this method, specific elastic and permeability matrices chosen based on the scaffold application can be achieved. Methods for comparing matrices for target matching are detailed in Appendix D.

Kang et al. [33] use a homogenization based topology optimization approach for the design of 3D unit cells of a tissue scaffold. The mechanical and mass transport environments were quantified using effective bulk modulus and isotropic diffusivity. Design targets were computed using Hashin-Shtrikman cross property bounds between bulk modulus and diffusivity for a given porosity [33]. Local microstructural topology optimization based on the SIMP method was used to for target optimization. An objective function for target stiffness (C^*) and target diffusivity (D^*) is formulated as follows:

$$minimize \quad f = w_1 \left(\frac{\boldsymbol{C}^H}{\boldsymbol{C}^*} - 1 \right)^2 + w_2 \left(\frac{D^H}{D^*} - 1 \right)^2 + w_3 f_{cubic} \qquad [27]$$

$$subject\ to \quad \phi_{lb} \leq \sum_{i=1}^{N} \frac{1 - \rho_i}{N} \leq \phi_{ub}, \qquad 0 < \rho_i \leq 1$$

The cubic error function f_{cubic} is defined to minimize the differences among the three normal components, three off-diagonal components, and three shear terms in the stiffness matrix. The lower and upper bounds on porosity are given by ϕ_{lb} and ϕ_{ub} respectively.

MMA was used to update the design variables and a nonlinear filtering technique was applied to the sensitivity derivatives to address checkerboard pattern issues and mesh dependencies. The results were unit cells with properties close to the cross property bounds, showing that unit cells can be tailored to meet various requirements for porosities from 30-60% [33].

In another study by Lin et al., a target matching method was developed to design a scaffold unit cells to have specified elastic and porosity properties, using a homogenization based topology optimization algorithm [14]. With the target material to be used for bone tissue engineering, it was shown that highly porous structures can be made that match human trabecular bone stiffness using biomaterials. In this study, MMA is used as the optimization solver, with the objective function a weighted summation of minimization of error between the target and homogenized stiffness matrix components. A porosity constraint is enforced. The objective function is defined as:

$$OBJ_n = \left\| C_{ijkl}^H - C_{ijkl}^* \right\|_{L_2} \qquad [28]$$

$$= \frac{1}{V} \int_V (C_{ijkl}^H - C_{ijkl}^*)^2 dV$$

$$n = 1,2,\dots,N \quad i,j,k,l = 1,2,3$$

The design variable is relative density and weighting factors are used to normalize the objective functions to the same scale. C_{ijkl}^* is the target stiffness tensor and C_{ijkl}^H is the homogenized stiffness tensor. The L_2 norm operator is defined as the square of the difference between target and homogenized stiffness components.

Because of the existence of non-unique solutions, the result is highly dependent on the initial material distribution in the design space. To address this problem, the design procedure

uses an initializing procedure to find a suitable initial material layout. In the initial loop, topology optimization is performed with a coarse mesh of initially uniform material distribution. The coarse result is then used as an initial guess for the main topology optimization which uses a much higher resolution mesh. It is suggested that a series of optimization trials be conducted with difference initial guesses to study the relation between initial guess and final topology.

2.6 Alternative to topology optimization

An alternative approach to the material layout problem is to define the topology *a priori* based on engineering knowledge. Instead of iteratively designing the architecture until the desired properties are reached, this ad hoc approach involves first designing the architecture and then computing its effective properties. In a study by Hollister et al., instead of using topology optimization, it is assumed that the basic unit cell structure consists of intersecting cylindrical pores and the pores have continuous connectivity [25]. A degradable bone tissue scaffold was then designed to meet conflicting design requirements.

Ad hoc and topology optimized design approaches for scaffold architecture were compared to theoretical bounds on stiffness in another study by Hollister et al. [30]. The topology optimization results here did not show great improvement over the ad hoc design with spherical voids. In the topology optimization approach, different initial guesses led to very dissimilar final designs, even with the same effective properties. As expected, these results show that the optimization did not generate global optima and the final design is initial guess dependent.

A possible solution to meet manufacturing and functional constraints is to develop a library of unit cells with a wide range of properties [25]. An advantage of having a restricted set of topologies is that scaffolds with heterogeneous property distributions can be designed by cells from the library, each satisfying continuous connectivity. All microstructures would provide a connected pathway for cell migration and nutrient flow. On the other hand, topology optimization schemes may not necessarily produce connected pores, unless specifically implemented as a constraint in the optimization model.

2.7 Hierarchical topology optimization

This section will review current methodologies to approaching the hierarchical topology optimization problem, drawing on theory described in the previous sections. As discussed in Chapter 1, bone tissue is a hierarchical structure, with features ranging in size from the nano-

scale to centimeters. The hierarchy in structure allows for large variation in function and physiology of bone [68]. It is a well held paradigm that tissue replacements should closely mimic the natural tissue structure and function. Thus, controlling the hierarchical features of an artificial scaffold can allow for the optimization of function and tissue regeneration [25]. The analysis of hierarchical lattice materials is demonstrated by Pasini et al. [69-72] as well as in the work described below.

A porous scaffold with structural hierarchy is proposed by Chen et al. to optimize tissue regeneration [73]. Chen et al. hypothesize that including hierarchy in scaffold is necessary to achieve the mechanical response of tissue. The premise of this work is the following: if the unit cell of a cellular material is called the first level of hierarchy, the mechanical properties of the first level can be deduced from its constituent materials. This can be conducted for multi-levels. For the Nth level structure, the $(k-1)^{th}$ level, where k=1...N, can be treated as a continuum media to study the kth level properties. It is assumed that the unit cell length scale at the $(k-1)^{th}$ level is much less than the kth level. The results show that as the hierarchical level number increases, porosity increases and strength decreases, approaching cortical bone Young's modulus and strength when using constituent material properties (that is, of individual trabeculae).

This hierarchical approach is applied in a study by Rodrigues et al., where topology optimization was used to determine material distribution and local material properties of a cellular structure. The method employed here uncouples the topology design problem into two scales. The outer (global) problem is concerned with the spatial distribution of material, and the inner (local) problem addresses the optimal design of the unit cells. At the global level, the design goal is the determination of the optimal distribution of material in space with variable relative density [74]. The global problem is defined as a minimum compliance design problem, formulated as a weighted average of compliance values for the case of multiple loads. To obtain a hierarchical structure, the problem is formulated such that the strain energy is maximized at each point of the structure. This pointwise maximization is treated as the inner subproblem. The global problem determines the macroscopic spatial distribution and the inner subproblem determines effective properties of the optimal microstructure. At each spatial location, the design of a unit cell is sought with a given density of material. The stiffness interpolation between void and the given material properties is found using SIMP as $C(\rho) = \rho^p C_{base}$. $C(\rho)$ is the stiffness

for a unit cell with a given relative density ρ, with penalty factor p and solid material stiffness C_{base}.

After initialization, subproblems are solved and the homogenized stiffness is computed for each element. The global problem is solved and a global displacement field is calculated. Each element is updated (by means of the design variable, relative density), and then new homogenized stiffness is calculated. A check for convergence is performed. Thus, the numerical procedure involves two finite element models: one discretized in the global domain and one discretized in the local domain. Local and global displacement fields are approximated with iso-parametric elements and design variables are interpolated as constant in each respective element. Because the local problems are independent, using parallel processing allows them to be solved simultaneously.

An improvement on this work was conducted by Coelho et al in 2007, with similar problem formulation but in three dimensions rather than two [39]. The optimization model works at two interconnected levels (global and local) to find the optimal structure and its material. Asymptotic homogenization is used to determine effective properties and SIMP based approach is used. Optimality conditions are approximated using finite element discretization at the local and global levels. Checkerboard patterns are addressed by a filtering technique based on a weighted average of design gradient values.

In 2010, a similarly formulated hierarchical topology optimization problem was solved, but a permeability constraint is introduced [75]. The problem again is formulated as a structural compliance minimization problem subjected to a material volume constraint, and subjected to local material constrains. The structure and its material are simultaneously optimized. The MMA is employed for the global problem, as it is capable of handling local material design constraints (such as manufacturing, symmetry, and permeability). The local problem is solved using a similar mathematical programming method called CONLIN, from which MMA is derived. In this study, a permeability constraint is enforced as a lower bound constraint, where permeability is calculated from the homogenized permeability tensor. Orthotropic symmetry on the tensor is enforced. Permeability control is found to lead to more convoluted solutions, which better resemble real trabecular bone patterns.

Further motivation for hierarchical design is that enhanced bone growth is found in random structures [76]. In hierarchical topology optimization, the microarchitecture of each unit cell is designed independently of its neighbour, resulting in a non-homogenous scaffold. This introduces heterogeneity throughout the structure, found to be a beneficial factor in bone ingrowth.

In summary, multi-objective optimization for both stiffness and permeability for bone tissue scaffolds has been explored by Hollister, Guest, Challis, et al. [13, 14, 25, 33, 53, 66] and methods have been developed that can produce unit cells close to the theoretical cross property bounds [33, 67]. Hierarchical topology optimization for bone tissue scaffolds has a strong biological motivation, and methods have been developed by Coelho, Rodrigues, Chen, et al. [39, 73-75, 77, 78] which demonstrate the capability of multi-scale modeling for target properties. One natural next step in exploring the computational design of bone tissue scaffolds is dictated by the gap in current literature: the multi-objective optimization of stiffness and permeability of a hierarchical bone tissue scaffold. Currently, no published work describes the combination of hierarchical topology design with multi-objective topology optimization for bone tissue scaffold design, the focus of this work.

Chapter 3: Hierarchical topology optimization algorithm

Based on the methods and theory described in Chapter 2 as well as previous algorithms reported in literature, a unique 2D hierarchical topology optimization routine is proposed in this chapter for the design of a bone tissue scaffold. The objective of the proposed methodology is the design of a scaffold that has stiffness close to that of bone and maximum permeability. This chapter will provide a description of each step of the algorithm and discuss the model assumptions. In Chapter 4, the methodology is applied to the design of a bone fracture fixation plate.

3.1 Algorithm structure

This section provides an overview of the proposed algorithm and respective assumptions. The procedure is divided into sequential material layout problems at two scales: (1) the topology of the implant, and (2) the topology of each unit cell to meet functional requirements at each location of the cellular material. Although some methods in literature perform these searches in parallel, this procedure involves designing each unit cell after the optimal topology of the scaffold is determined. The SIMP method is used to interpolate target material properties for each unit cell based on the optimal material distribution found in the implant optimization stage. The optimization procedure is performed using MATLAB, in combination with ANSYS for finite element analysis. A simple schematic depicting the overall procedure is shown in Figure 12, with a more detailed flowchart shown in Figure 13.
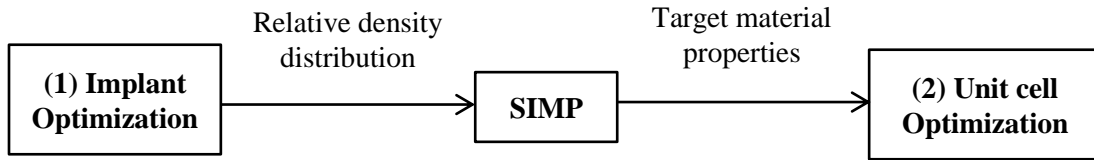
Figure 12: General schematic of optimization procedure.

3.1.1 Initial guess

The convergence of topology optimization problems can be highly dependent on the initial material layout in the design space. Due to the nonexistence of a unique solution to the optimal topology of a unit cell for maximum stiffness and permeability, local minima for the objective function may be found with different initial material distributions. In both stages of the proposed procedure, a uniform distribution of material within the design space is chosen as an initial guess.
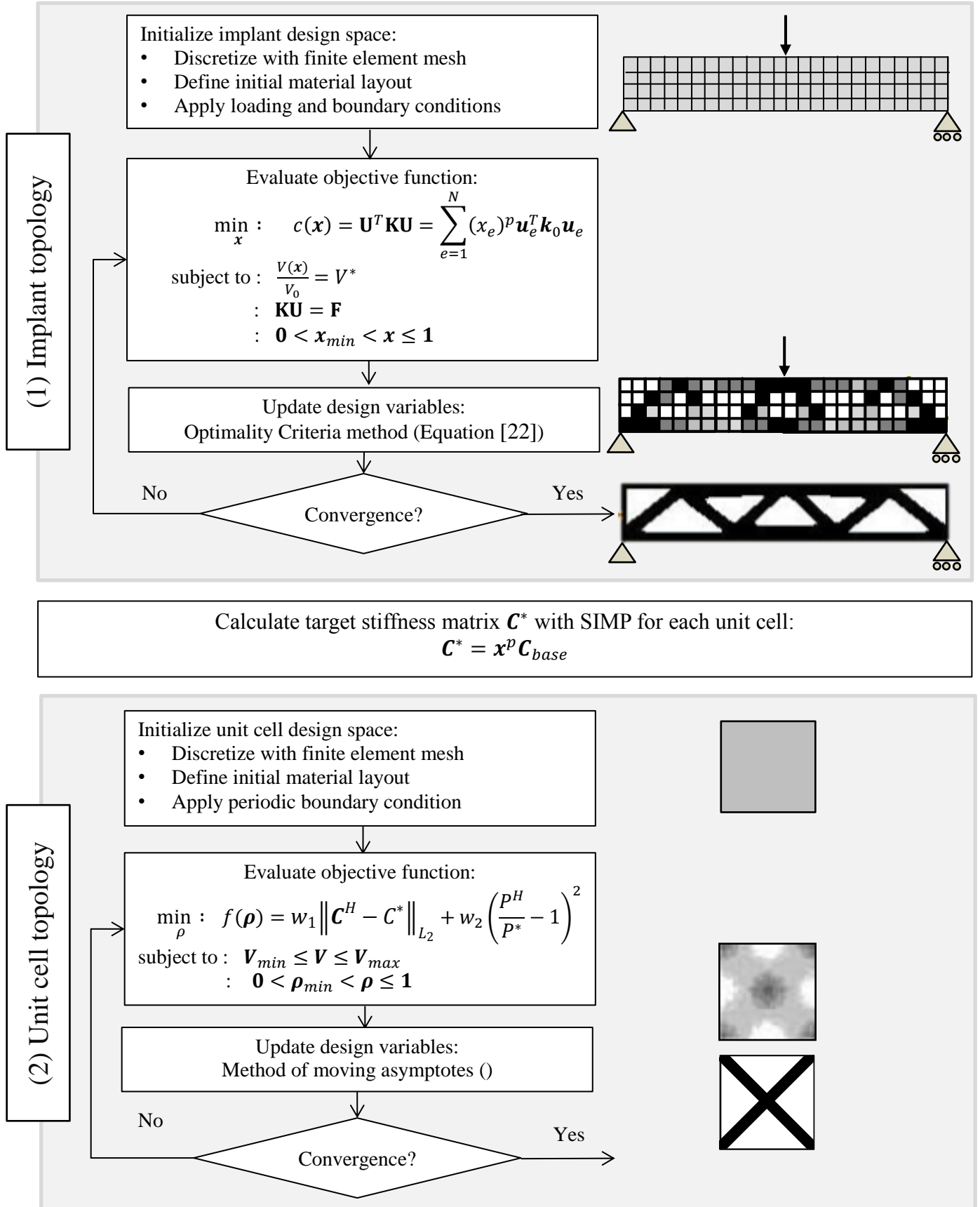
(1) Implant topology

Initialize implant design space:
- Discretize with finite element mesh
- Define initial material layout
- Apply loading and boundary conditions

Evaluate objective function:

$$\min_{x} : \quad c(x) = \mathbf{U}^T \mathbf{K} \mathbf{U} = \sum_{e=1}^{N} (x_e)^p \boldsymbol{u}_e^T \boldsymbol{k}_0 \boldsymbol{u}_e$$

$$\text{subject to} : \quad \frac{V(x)}{V_0} = V^*$$
$$: \quad \mathbf{KU} = \mathbf{F}$$
$$: \quad \mathbf{0} < \boldsymbol{x}_{min} < \boldsymbol{x} \leq \mathbf{1}$$

Update design variables:
Optimality Criteria method (Equation [22])

Convergence?   No   Yes

Calculate target stiffness matrix $\boldsymbol{C}^*$ with SIMP for each unit cell:
$$\boldsymbol{C}^* = \boldsymbol{x}^p \boldsymbol{C}_{base}$$

(2) Unit cell topology

Initialize unit cell design space:
- Discretize with finite element mesh
- Define initial material layout
- Apply periodic boundary condition

Evaluate objective function:

$$\min_{\rho} : \quad f(\boldsymbol{\rho}) = w_1 \left\| \boldsymbol{C}^H - C^* \right\|_{L_2} + w_2 \left(\frac{P^H}{P^*} - 1 \right)^2$$

$$\text{subject to} : \quad \boldsymbol{V}_{min} \leq \boldsymbol{V} \leq \boldsymbol{V}_{max}$$
$$: \quad \mathbf{0} < \boldsymbol{\rho}_{min} < \boldsymbol{\rho} \leq \mathbf{1}$$

Update design variables:
Method of moving asymptotes ()

Convergence?   No   Yes

Figure 13: Hierarchical topology optimization flowchart.

3.1.2 Filtering

A filter to modify objective function sensitivity is applied to ensure mesh-independency and avoid a checkerboard pattern. In the topology optimization routine, the gradients are calculated for each mesh element independently of one another. The sensitivity of each element is then recomputed taking into account a weighted average of the neighboring element sensitivities within a fixed range. This is a heuristic method of filtering but it is computationally efficient and simple to implement.

3.1.3 Unit cell symmetry constraint

It is advantageous and convenient to design unit cells of a scaffold with an imposed symmetry constraint. Computational effort can be reduced by designing one quarter of a unit cell based on symmetry assumptions. Additionally, structures without square symmetry may have directions with low material properties such as stiffness or permeability, and weak directions may not be desirable. A symmetry constraint is a method to ensure that the stiffness and permeability do not change in both normal directions. This is included in the unit cell topology optimization as a weighted term of the following objective function:

$$w * \left(\frac{C_{22}^H}{C_{11}^H} - 1 \right)^2 \qquad [29]$$

In a study by Rose et al., scaffolds were shown to have enhanced cell and tissue regeneration both in vitro and in vivo with a random porous structure, as opposed to a periodic structure [76]. In hierarchical topology optimization, the microarchitecture of each unit cell is designed independently of its neighbour, resulting in a non-homogenous scaffold. This introduces anisotropy in the scaffold as a whole, with unit cells conveniently designed with a symmetry constraint.

3.2 Implant topology optimization (1)

The first stage of optimization in the hierarchical technique is to determine an optimal material layout for an implant with minimal compliance (or strain energy), to reduce the difference between the strain energy of the base material (Ti6Al4V) and bone. Bone is much less stiff than titanium alloys used in implant design. The objective function $c(x)$ to minimize compliance using a power based topology optimization approach is formulated as follows:

$$\min_{\boldsymbol{x}}: c(\boldsymbol{x}) = \boldsymbol{U}^T \boldsymbol{K} \boldsymbol{U} = \sum_{e=1}^{N} (x_e)^p \boldsymbol{u}_e^T \boldsymbol{k}_0 \boldsymbol{u}_e$$

$$subject\ to\ \ :\ \ \frac{V(\boldsymbol{x})}{V_0} = V^*$$

$$:\ \ \mathbf{KU} = \mathbf{F}$$

$$:\ \ \mathbf{0 < x_{min} < x \le 1}$$

where $\boldsymbol{x}$ is the design variable (relative density) of each element e, **U** is displacement and **K** is stiffness. The optimization scheme is governed by the structural elasticity equation $\mathbf{KU = F}$. This formulation is widely used in literature for minimizing compliance, specifically in the 99 line topology optimization code developed by Sigmund (2001) which is used as a starting point in this analysis.

A volume fraction constraint is applied as an equality constraint, with target volume V^* defined by the user. Volume fraction is measured as the ratio of solid material $V(\boldsymbol{x})$ to the size of the design domain V_0. An inequality constraint on the design variable x is imposed to restrict values of relative density to lie between a value close to zero and 1. A small number, 10^{-3}, is chosen as the minimum value of x to avoid singularities in the finite element calculations. Otherwise, re-meshing would be required to exclude void elements. A penalty factor $p = 3$ is chosen, based on the suggestion by Sigmund et al. to ensure convergence [58]. The effect of changing penalty factor p is discussed in section 3.4.

Topology optimization at the implant level is described below, as depicted in Figure 13. A design space is first defined with both the displacement and stiffness fields discretized without changing mesh. Identical four-node quadrilateral mesh elements are used, and a uniform relative density distribution is initially defined. Material properties of the solid phase are defined with Young's modulus and Poisson's ratio, which are used to calculate the material stiffness. Plane stress is assumed in this two-dimensional analysis. Loading and boundary conditions are specifically applied depending on the expected physiological loading of the implant. The topology optimization procedure is highly sensitive to loading and boundary conditions, so careful selection is essential.

The iterative procedure begins with the evaluation of the objective function for the initial material distribution within the design space. The sensitivity of the objective function is calculated, and a filtering technique is applied to smooth the gradients, as described in section

3.1.2. The design variables are updated based on the filtered sensitivities, according to the Optimality Criteria method described in section 2.3.2. A convergence check is performed, which evaluates the maximum change in relative density for each element from its current value to its value from the previous design. Convergence is found when the maximum change in relative density of all elements is below a defined threshold, in this case 0.02. When the design variables have stabilized within the prescribed tolerance, the optimal material distribution is achieved.

With the optimal relative density for each unit cell determined, the target stiffness at each location of the implant is calculated. A relative density of 1 indicates that the desired stiffness of that unit cell is equal to the predefined base material stiffness. Similarly, a relative density near zero indicates that no stiffness is required at that location. The SIMP relation is used to interpret intermediate values of relative density as material properties for each unit cell:

$$\boldsymbol{C}^* = x^p \boldsymbol{C}_{base} \tag{30}$$

where penalty factor $p = 3$, $\boldsymbol{C}^*$ is the interpreted stiffness matrix of a unit cell with a given relative density x, and $\boldsymbol{C}_{base}$ is the solid material stiffness. With target stiffness for each location of the implant defined, unit cells can be specifically designed to match these local requirements in the next stage of optimization.

3.3 Unit cell topology optimization (2)

The second stage in the topology optimization routine is to design unit cells to achieve local target stiffness and permeability, based on bone ingrowth requirements. Each unit cell is designed independently of surrounding unit cells. The objective function is formulated as follows:

$$\min_{\rho} : \quad f(\boldsymbol{\rho}) = w_1 \left\| \boldsymbol{C}^H - \boldsymbol{C}^* \right\|_{L_2} + w_2 \left(\frac{P^H}{P^*} - 1 \right)^2 + w_3 \left(\frac{C_{22}^H}{C_{11}^H} - 1 \right)^2$$

$$subject\ to : \quad \Phi_{min} \leq \Phi \leq \Phi_{max}$$

$$: \quad 0 < \rho_{min} < \rho \leq 1$$

Where $\boldsymbol{\phi}$ is porosity of the unit cell and $\boldsymbol{\rho}$ is relative density of each mesh element. The first term of the minimization problem is difference between target stiffness and effective stiffness of the unit cell. The L_2 norm is calculated as the square of the difference between target ($\boldsymbol{C}^*$) and homogenized ($\boldsymbol{C}^H$) components. The target stiffness matrix is determined from Equation [30]. The effective stiffness is calculated using asymptotic homogenization, implemented with

ANSYS mesh and finite element solver. The second term of the objective function is the squared difference between target and effective permeability of the unit cell. Effective permeability is calculated using Weissberg's formula (Equation [5]). The target permeability is also calculated using Weissberg's formula, which is solely a function of porosity, ϕ. The acceptable range of porosity for bone ingrowth is 60-80%, so the maximum porosity (80%) is used to determine the target permeability. The third term in the objective function ensures square symmetry of the unit cell, as described in section 3.1.3. The acceptable range of porosity is enforced using an inequality constraint, where ϕ_{min}=60% and ϕ_{max}=80%. An inequality constraint is also used to ensure that the relative density of each mesh element is between ρ_{min}=**0.001** and **1**.

The design space is initialized with a uniform finite element mesh of four-node quadrilateral elements. In-plane stress is assumed. A periodic boundary condition is applied to the unit cell for the calculation of effective stiffness properties. The iterative procedure begins with evaluating the objective function for the initial material distribution, based on calculation of effective stiffness and permeability properties. The method of moving asymptotes is used to update the design variables, as described in section 2.3.2. A convergence check is performed to evaluate the maximum change in relative density for each element, from its current value to its value from the previous design. Convergence is reached when the maximum change in relative density of all elements is below a prescribed tolerance of 1%. This procedure is conducted for each unit cell, which can then be mapped to their respective locations within the implant structure. Further discussion on unit cell mapping is found in section 4.4.

3.4 Model validation

To verify the validity of the topology optimization routines developed here, it is essential to qualitatively and quantitatively compare the numerically determined results to closed-form solutions from benchmark problems of optimal material layout [59]. A set of well-known benchmarks of optimum structural layouts are the Michell trusses, which are theoretically solved optimal truss structures for bending. Among the various benchmark problems, Figure 14 and Figure 15 show two examples of an initialization of the design space with the relative optimal material distribution.

Quantitative verification of a solution consists of the following procedure: (a) for a given problem, numerically derive the optimal topology for various volume fractions and various

numbers of mesh elements, (b) calculate structural volume for each solution, (c) extrapolate the volume for zero volume fraction and infinite number of elements, and finally (d) compare this extrapolated value with that calculated analytically for exact benchmarks [79]. In a study by Kikuchi et al., the inverse homogenization method with SIMP for topology optimization that is used in this thesis was verified for the generalized layout problem by showing it can reproduce the Michell truss shown in Figure 14 [59]. As shown in Figure 14, a bending force F must be optimally transferred to a non-deforming circular support by constructing some truss structure.
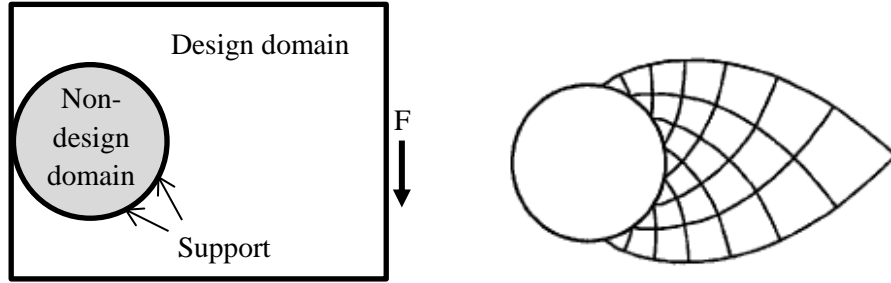
Figure 14: Design space initialization and analytical solution of the Michell truss [59].

A qualitative examination of a solution for a second Michell truss structure (Figure 15) was conducted. Table 3 shows the effect of mesh resolution and relative density on the optimal design. A change in topology can be observed with an increased mesh resolution, indicating that it is essential to use a mesh density high enough to avoid mesh dependency. Table 4 shows the influence of the penalty factor p. It is observed that a low penalty factor ($p = 1$) yields optimal designs where many mesh elements have intermediate values of relative density. It is also observed that with a high penalty factor, the design procedure may converge too quickly to a solid-void design, finding a local minimum which is overly sensitive to the choice of initial design. Numerical instabilities are found with higher penalty factors ($p > 4$) due to ill conditioned matrices.
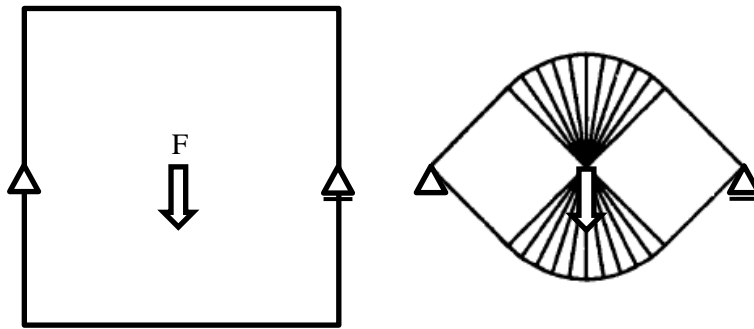
Figure 15: Design space initialization (left) and analytic solution (right) of the Michell truss [59].

The analytical solutions of Michell trusses have an infinite number of bars; however finite solutions are found numerically. One reason for the limited number of bars is the type of mesh element used. Using uniform square elements restricts material distribution because it necessitates a very fine mesh in order to represent the sharp corners between the bars, as shown in Figure 15. However, the use of square elements is very convenient for simplicity of programming and finite element analysis. The sensitivity filtering that is imposed to reduce mesh dependency also reduces the development of detailed features, but it is necessary for convergence. From Table 4, it is apparent that higher penalty factors can result in a topology with more bars, however as discussed above, numerical instabilities are observed with $p > 4$. Therefore, it is valid to use the proposed topology optimization procedure with $p \leq 4$ to achieve meaningful results, althoughit is important to note that the limitations of the procedure can be attributed to mesh resolution, element type, and filtering.

Table 3: Effect of mesh resolution and relative density on the topology optimization of a Michell truss problem, with penalty factor p=3.
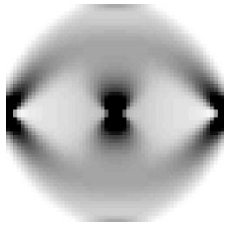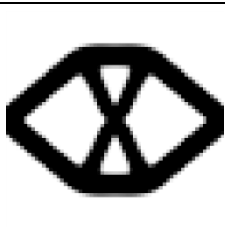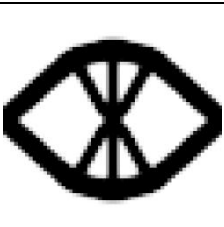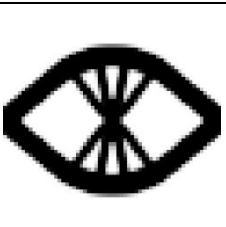
	Relative density		
Mesh resolution	**20%**	**30%**	**40%**
40x40			
60x60			
80x80			

Table 4: Effect of penalty factor p on the topology optimization of a Michell truss problem. Mesh size is 60x60 and relative density is 30%.

p		p		p	
1		2		3	
4		5		6	

Chapter 4: Results

This chapter shows the application of the hierarchical topology optimization routine described in Chapter 3 to the design of a cellular bone fracture fixation plate. First, the material distribution of the plate is determined. Secondly, a sample of unit cells for various locations throughout the plate are designed for target stiffness and permeability based on bone ingrowth requirements (Figure 16). Finally, the mapping of unit cells into the plate structure is illustrated and discussed.
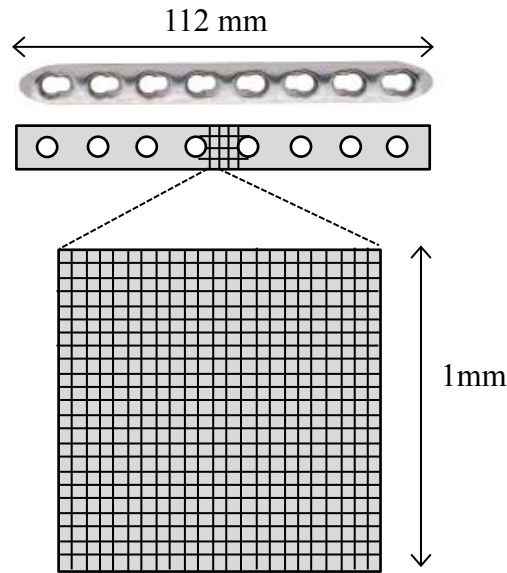
Figure 16: Schematic of fracture fixation plate optimization scales [80].

4.1 Fracture fixation plate design motivation

A compression fracture fixation plate provides a locking force across a fracture site to which it is applied. The plate is attached to bone fragments using screws, resulting in tension of the plate, and compression at the site (parallel to the plate). The purpose of the plate is to provide increased stability of the fractured bone fragments, reduce the gap space that must be healed by new forming tissue, protect the blood supply in the area, and prevent sliding by increasing friction. The plate alone is not necessarily designed to resist torsion well. The stiffness of the plate should be close to that of bone with sufficient strength. Often, Ti-6Al-4V or stainless steel (316L) is used for the plate. These are both biocompatible materials; however, titanium offers a higher strength to stiffness ratio and is used here [81].

54
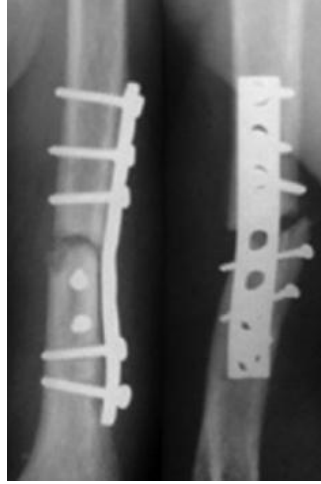
Figure 17: Lateral view of humerus with dynamic fracture fixation plate and screw system [82].

Ongoing concerns with fracture fixation plates are (1) excessive stiffness resulting in stress shielding, and (2) osteoporosis of underlying bone. The resulting decrease in bone mass and density increases risk of re-fracture at the site [36]. Osteoporosis beneath a fracture fixation plate can be caused by disruption of blood flow to the fracture site. Stress shielding results from the mismatch of mechanical properties causing delayed callus formation and bone healing. The Young's modulus of cortical bone is approximately 20 GPa, compared to 110 GPa for Ti-6Al-4V. The porous nature of a cellular fracture fixation plate reduces disruption of blood flow to the bone, while mechanical properties can be specifically tailored at the unit cell level to match those of the local tissue to reduce stress shielding.

4.2 Plate topology optimization

The plate design space is initialized based on the dimensions of a small fragment locking compression plate system by Synthes, Inc [80]. For an 8-screw plate with 3.5mm hole diameter, the plate length is 112mm and width is 12mm. It is reported that a compression plate should provide approximately 600N of compressive force [35]. In this analysis, completely in-plane loading is assumed, and 600N is distributed as a tensile force on the outer face of each screw hole, as shown in Figure 18. Symmetry is exploited and only half of the plate is modeled, using a symmetric boundary condition (right side in Figure 18).
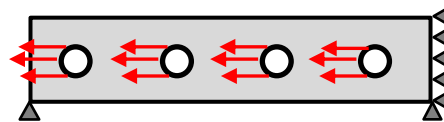
Figure 18: Schematic of loading and boundary conditions for half of the fracture fixation plate.

The mesh resolution was varied and finally chosen as 48 elements by 448 elements. At higher mesh resolutions, no difference in topology was observed. One mesh element is equivalent to 0.25mm in length and width. Each hole is prescribed to have void elements with a solid material boundary for screw threading. Elsewhere, the initial material distribution is uniformly 50% relative density. The target stiffness for the implant is that of the in-plane tensile stiffness of cortical bone: approximately 20092 N/mm. This was determined by a tensile stiffness analysis conducted in ANSYS for a solid plate with cortical bone properties ($E = 20GPa$, $v = 0.3$). Table 5 shows the optimal Ti-6Al-4V plate topologies found using a 50% material fraction equality constraint, with various penalty factors used to interpolate material properties. The first entry in the table shows a solid plate with 8 screw holes for comparison. Table 6 summarizes the strain energy and stiffness for the optimal plates, calculated in ANSYS. The solid plate has significantly higher stiffness than cortical bone, and is an order of magnitude greater than the target. Intuitively, lower stiffness is observed with a 50% material fraction constraint. By using less material and allowing for intermediate values of relative density (e.g. with $p = 1.1$), a titanium plate can be designed with stiffness much closer to cortical bone.

Table 5: Optimal plate topologies with 50% material fraction.

Design	Optimal topology
(a) Solid	
(b) $p = 3$	
(c) $p = 1.25$	
(d) $p = 1.1$	
(e) $p = 1$	

Table 6: Strain energy and stiffness for 50% material fraction plates.

Design	Material fraction	Penalty factor, p	Strain energy (N/mm)	Tensile stiffness (N/mm)
(a) Solid	94.11%	N/A	10974	204857
(b) $p = 3$	50%	3	4494	83905
(c) $p = 1.25$	50%	1.25	3215	60013
(d) $p = 1.1$	50%	1.1	1715	32021
(e) $p = 1$	50%	1	783	14621

For a 50% material fraction constraint, it appears that the penalty factor should lie between 1 and 1.1 in order to achieve the target stiffness of cortical bone. Changing the material fraction constraint can also result in plates with stiffness closer to the target. For example, the optimal plates with a 45% material fraction constraint are shown in Table 7 and Table 8, with the penalty factors of the the 50% volume fraction plates. Table 8 shows that with $p = 1.1$, plate stiffness is 18910 N/mm, which is approximately 6% less than that of cortical bone. The adjustment of input parameters allows for fine tuning of the optimal results, so as to achieve target stiffness. Appendix D shows optimal topologies obtained for a range of material fractions.

Table 7: Optimal plate topologies with 45% material fraction.

Design	Optimal Topology
(a) Solid	
(b) $p = 3$	
(c) $p = 1.25$	
(d) $p = 1.1$	
(e) $p = 1$	

Table 8: Strain energy and stiffness for 45% material fraction plates.

Design	Material fraction	Penalty factor, p	Strain energy (N/mm)	Tensile stiffness (N/mm)
(a) Solid	94.11%	N/A	10974	204857
(b) $p = 3$	45%	3	4080	76161
(c) $p = 1.25$	45%	1.25	2654	49555
(d) $p = 1.1$	45%	1.1	1013	18910
(e) $p = 1$	45%	1	620	11586

In general, a lower penalty factor p yields more graded material distribution in the optimal design, which can be realized by designing further at the unit cell level for each location, to achieve target material properties. The SIMP relation is used to interpolate effective material properties from intermediate values of relative density. This allows for new areas of the design space to be accessible, beyond what is achievable with completely solid material. Design (d) in For a 50% material fraction constraint, it appears that the penalty factor should lie between 1 and 1.1 in order to achieve the target stiffness of cortical bone. Changing the material fraction constraint can also result in plates with stiffness closer to the target. For example, the optimal plates with a 45% material fraction constraint are shown in Table 7 and Table 8, with the penalty factors of the the 50% volume fraction plates. Table 8 shows that with p=1.1, plate stiffness is 18910 N/mm, which is approximately 6% less than that of cortical bone. The adjustment of input parameters allows for fine tuning of the optimal results, so as to achieve target stiffness. Appendix D shows optimal topologies obtained for a range of material fractions.
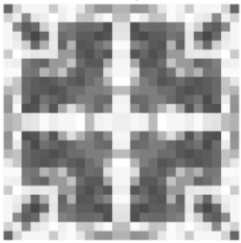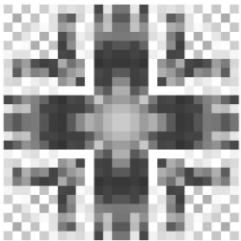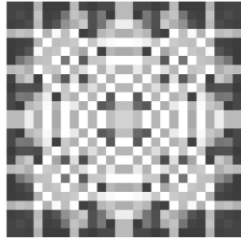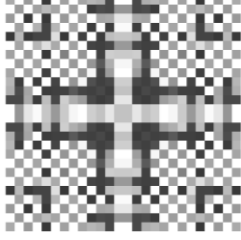
Table 7 is chosen as the optimal plate topology, and is further designed at the unit cell level in section 4.3.

4.3 Unit cell topology optimization

The unit cell optimization procedure was conducted for a range of input parameters. Target stiffness properties were used based on relative densities ranging from 10% to 90%, in increments of 10%. Penalty factor p was also varied between 1 and 3 in increments of 0.5, with the goal of achieving a completely solid void design. Each combination of penalty factor and relative density was repeated three times to observe the repeatability of the procedure. Stiffness and permeability components of the object function were initially weighted equally. A mesh size of 26x26 elements was used.

Convergence to an optimal topology was challenging to find. As reported in literature, convergence using the method of moving asymptotes is often not found [63]. Adjusting the MMA parameters, including step length for moving the asymptotes, were ineffective in yielding converging results. The best convergence was found with target stiffness properties determined by a relative density of 60%. As shown in Table 9, stiffness can be found within the range of 3-13% of this target, and permeability is found within 0.5-3.5%. Porosity is also within the acceptable range of 60-80%. Appendix E shows further optimal unit cell designs at a mesh resolution of 26x26 elements as well as 16x16 elements.

Table 9: Optimal unit cells with target stiffness determined by a relative density of 60%.

	Porosity	p	% Difference in the stiffness matrix components			% Difference in permeability
	65.23	1	-5.52 4.80 0	4.80 -5.52 0	0 0 2.14	-0.45
	65.77	1.5	-10.98 5.16 0	5.16 -10.98 0	0 0 2.92	-1.42
	65.50	2	-13.72 -3.87 0	-3.87 -13.72 0	0 0 -6.53	-0.91
	66.95	2.5	-13.17 -10.22 0	-10.22 -13.17 0	0 0 -8.60	-3.46

It was observed that higher penalty factors lead to more checkerboard patterns in the optimal design. The convergence to an optimal design with properties in the approximate range of the target was achieved; however regions of disconnected material within the unit cells and regions of intermediate material properties are present. An attempt to enforce connectivity between unit cells was made by prescribing certain regions of the design space to be solid, and these regions were not iteratively updated. With this constraint, a unit cell can be found with a percent difference in permeability of -2.35%, and percent difference in components of the stiffness matrix less that 5.5%. However, a completely solid-void topology was not achieved (Figure 19). Material tended to distribute uniformly throughout the unrestrained regions of relative density. Further suggestions for enforcing connectivity are discussed in Chapter 5.

Figure 19: Prescribed regions of material (dark grey) to ensure connectivity between unit cells.

An optimal unit cell that has a maximum percent difference in stiffness of 7.43% and a 1.43% difference in permeability was compared to the Hashin-Shtrikman theoretical bounds of bulk modulus and diffusivity (Table 10).

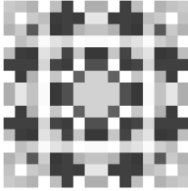Table 10: Optimal unit cell compared against Hashin Shtrikman bounds.

	Porosity	p	% Difference in the stiffness matrix components			% Difference in permeability
	65.79	2	-7.43 -1.44 0	-1.44 -7.43 0	0 0 -1.56	-1.43

Figure 20 shows that the effective bulk modulus for this unit cell falls beneath the theoretical bounds; however, effective permeability lies well outside the predicted maximum value. This may be indicative of an error in calculating permeability solely as a function of porosity. The error may be reduced by using a more robust method to calculated permeability, which also takes into account the geometric features of the unit cell. Modification to the permeability calculation method are further discussed in Chapter 5.
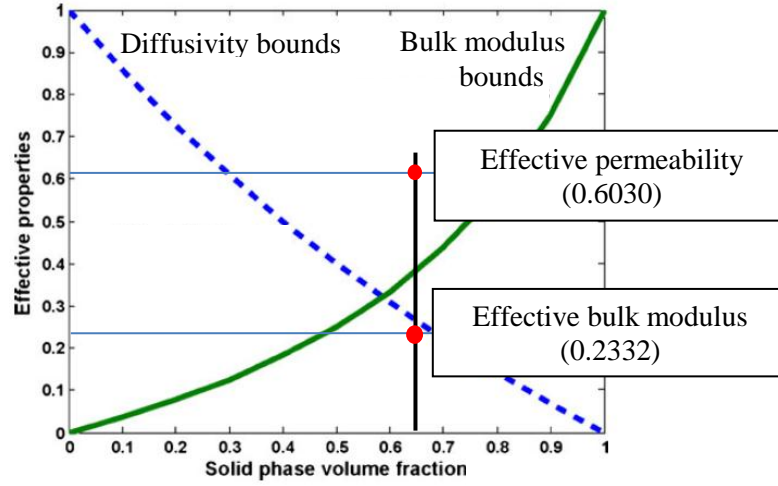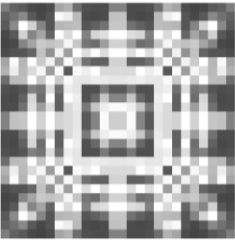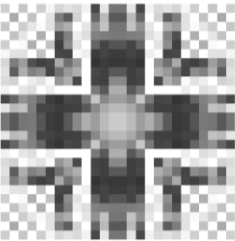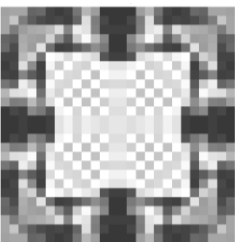
Figure 20: Comparison of optimal unit cell effective properties to theoretical bounds [33].

It was found that the optimal topologies found were highly dependent on the initial material distribution. This is illustrated in Table 11, where three different optimal topologies were found for given input parameters.

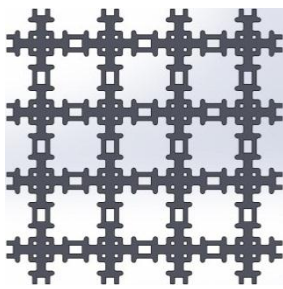Table 11: Unit cells with varying optimal topologies from same initial parameters.
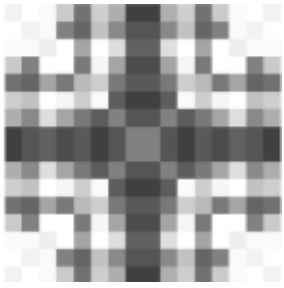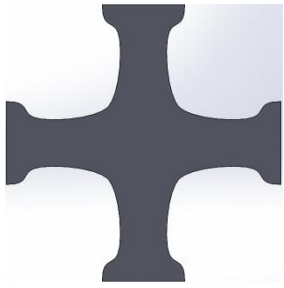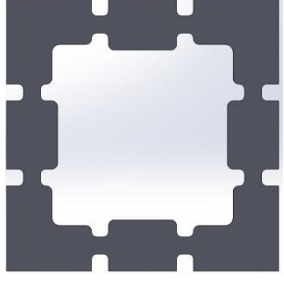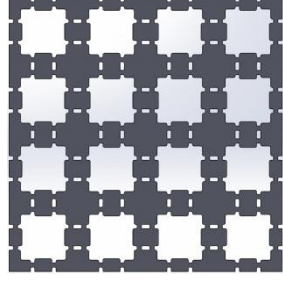
	Porosity	p	% Difference in the stiffness matrix components			% Difference in permeability
	64.34	1.5	-13.52 -3.61 0	-3.61 -13.52 0	0 0 0.32	1.19
	65.77	1.5	-10.98 5.16 0	5.16 -10.98 0	0 0 2.92	-1.42
	65.15	1.5	-12.78 -0.01 0	-0.01 -12.78 0	0 -100 6.72	-0.30

4.4 Mapping of unit cells

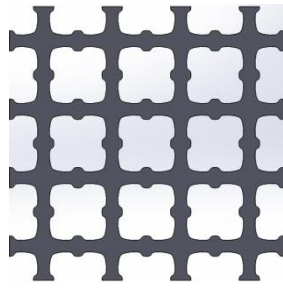This section discussed the procedure of mapping unit cells into the optimal implant topology domain. As stated in Chapter 2, the optimal scaffold environment for bone ingrowth has pore sizes of 50-400 microns and is 60-80% porous, where the porosity constraint is addressed in the unit cell optimization procedure. Theoretically, cell size can be tailored to meet pore size constraints during the procedure of mapping unit cells onto the optimal plate topology. Practically, manufacturing constraints on minimum allowable feature size govern the mapping procedure. Limits on the smallest possible pore and strut size determine the allowable unit cell dimensions. Currently, the nominal minimum strut size is approximately 200 microns for the additive manufacturing technique Electron Beam Melting. To address these constraints, instead of representing each mesh element as one unit cell, target material properties can be averaged over a region that is the size of the smallest manufacturable cell. For example, assuming the minimum cell length is 1mm and the mesh element length is 0.25mm, 1mm square unit cells are mapped to the implant based on the average relative density over a 4x4 element region.

To create implant models for manufacturing, computer-aided design (CAD) can be used to construct the optimized unit cells as solids. Table 12 shows three optimal unit cells that have been recreated using SolidWorks CAD Software. Refined boundary interpretation methods, such as the level set method [83] can be used to translate the optimal material distribution to a solid-void unit cell topology. However, due to low mesh size and prevalence of a checkerboard pattern in the results shown, the implant topology is interpolated heuristically for simplicity. A tessellation of each unit cell is also shown to illustrate the respective scaffold topologies. Figure 21 shows a CAD model of an optimized implant, prior to mapping of unit cells, with solid material temporarily representing areas of relative density greater than ~20%, and all other regions considered void. An example of the mapping procedure is shown in Figure 22-Figure 24. Once the procedure is capable of optimizing unit cells to meet target properties based on the entire range of relative densities (from 0-100%), the entire implant can be mapped by this method.

Table 12: CAD representation of optimal unit cells with tessellation.

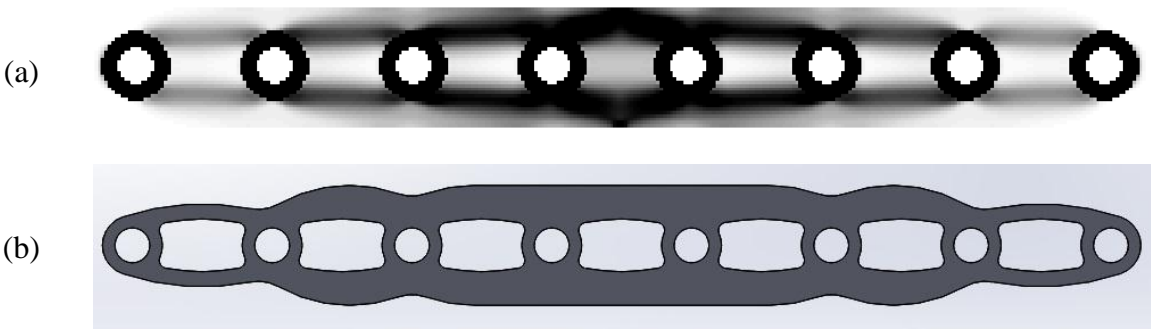|	Optimized unit cell	CAD unit cell	Tesselation
1			
2			
3			

(a)

(b)

Figure 21: CAD representation of optimized implant (material fraction 45%, p=1.1).

0.96	0.94	0.92	0.89
0.72	0.69	0.66	0.63
0.48	0.46	0.43	0.41
0.36	0.34	0.32	0.31

(a)   (b)   (c)
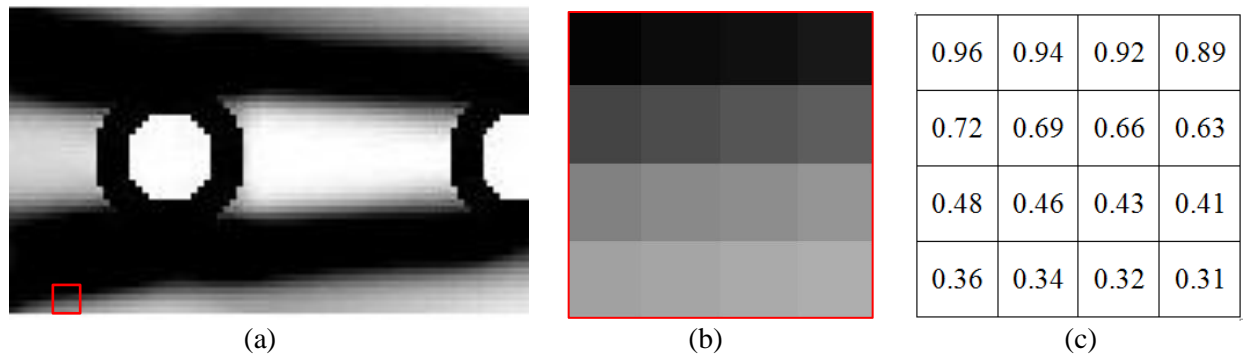
Figure 22: (a) Optimized implant material layout where 1mm x 1mm region (b) is highlighted in red, with mesh element relative density shown in (c).

(a)   (b)   (c)

Figure 23: (a) 1mm x 1mm region of optimal material distribution, with average relative density 60%. (b) 1mm x 1mm region of uniform relative density 60%. (c) Optimal unit cell with target material properties based on relative density of 60%.

(a)   (b)
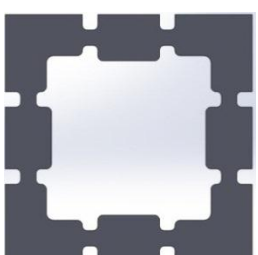
Figure 24: (a) CAD model of Figure 22 (a). (b) Mapping of optimal unit cell.

Effective permeability and stiffness were calculated for the CAD unit cells shown in Table 12 and the weighted objective function combining stiffness and permeability for each design was computed. The value of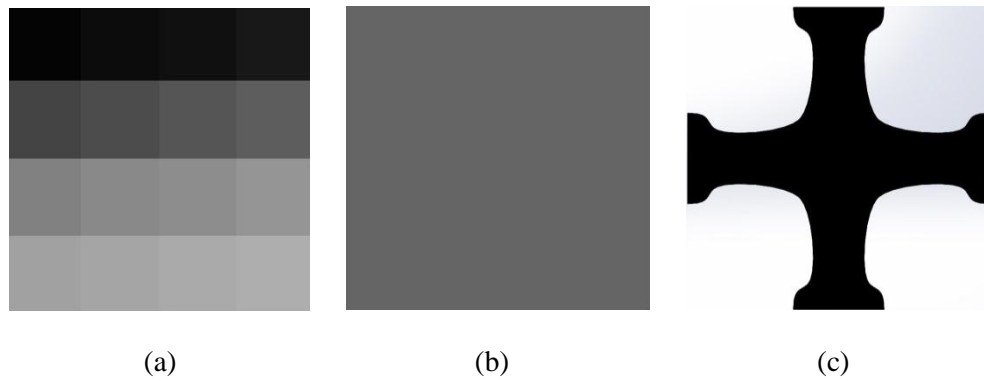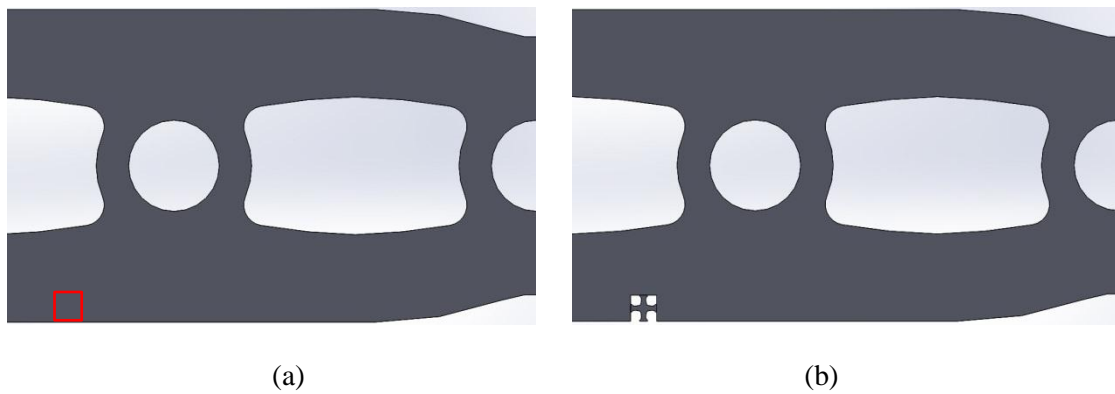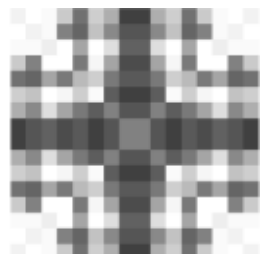 the weighted objective function for each CAD design was compared to its respective optimal unit cell design. Table 13 shows the optimal and CAD unit cells, and the percent difference between the values of the weighted objective function in each case. Sample calculations are shown in Appendix G, including how the percent difference is assessed. The large discrepancies in objective function value show that the CAD models of the optimized unit cells are not the best approximations. This can be attributed to the heuristic method used to interpret the optimal material distribution into a solid-void topology. Error may result from the translation of grey areas into a defined region of solid material. As previously discussed, by improving filtering and mesh size, the occurrence of checkerboard patterns will be reduced and a more distinct solid-void boundary is expected. This will allow for a more accurate representation of the optimal unit cell using CAD.

Table 13: CAD unit cell properties compared to targets.

	Optimized unit cell	CAD unit cell	Difference in objective function
1			96.85%
2			57.81%
3			95.65%

Chapter 5: Discussion and Conclusion

5.1 Summary

The capabilities and limitations of the proposed hierarchical topology optimization routine for the design of a bone tissue scaffold were demonstrated in Chapter 4. The first stage of the topology optimization shows convergence to optimal solutions for the minimization of compliance. Several optimal fracture fixation plate topologies were designed as a demonstration of the procedure. It was shown that by varying the penalty factor p and allowing for intermediate material properties between solid and void material, the design space is expanded. That is, for the same total amount of material, a large range of stiffness properties can be achieved and can be tailored to match the nonhomogeneous properties of bone. Optimal plate designs with intermediate material properties can be realized with multi-scale design by specifically tailoring a unit cell to meet the functional requirements of a given location. The multi-objective design of unit cells for targeted stiffness and permeability is based on bone ingrowth requirements. Optimization convergence is not always found at the unit cell level, and several improvements to the procedure are suggested below. However, with the target properties based on a relative density of 60%, optimal unit cells can be found within the range of 3-13% of desired stiffness and within 0.5-3.5% of desired permeability. CAD models of a sample of three unit cells were created to illustrate the next step towards manufacturing. A large discrepancy between target properties and proposed CAD model properties was found. Accurately translating the optimal unit cells to CAD models will require a finer mesh with more effective filtering imposed during optimization so that solid-void boundaries are clearly identified.

5.2 Discussion

Several adjustments can be made to the proposed procedure to improve convergence and reduce discrepancy between target and achieved properties. As shown in Figure 20, the method used to calculate permeability results in values that lie outside of theoretical bounds with stiffness, indicating a possible error in the calculation. Currently, permeability is determined using Weissberg's formula and is solely a function of porosity. A more sophisticated method for calculating effective permeability should be implemented, such as Stokes flow homogenization, which takes into account the geometry of the unit cell (section 2.1.2). It is hypothesized that

using Stokes flow homogenization may alter calculations for the permeability objective function and its sensitivity, improving problem convergence.

It is also apparent that a more effective filtering technique is required at the unit cell level. The sensitivity filtering method described in section 3.1.2 is highly effective with the optimality criteria method used in the first stage of optimization. However, it is less effective at the unit cell level and checkerboard patterns are often observed. There are other filtering techniques available that should be explored for possible improvement of this stage. For example, limitations can be imposed on the allowable variation in density distribution. Restrictions to the gradient can be imposed with pointwise bounds on the derivatives of relative density with respect to location in the mesh. Also, limits on the perimeter of mechanical elements in the design space can prevent solid material from appearing separately from the main structure. These techniques would have to be specifically catered to this design problem, but can potentially reduce checkerboard patterns.

It is observed that the optimal material distribution in the unit cell design space is highly dependent on the initial material distribution at the beginning of the optimization. This dependency is not necessarily a drawback in this case, because many local minima of the function may exist that all exhibit target material properties. The additional variation in topology is advantageous in that many different optimal unit cells can be mapped to the implant topology and a less periodic pattern is preferable for bone ingrowth.

Connectivity of material within the unit cell can be imposed using available software packages on the market, such as the visualization toolkit image-processing library (*vtkPolyData-ConnectivityFilter*) by Kitware, Inc. This software is used in the iterative design of unit cells by Lin et al [14] to ensure inner structure connectivity. One way that this software can be used is to identify the largest connected region in the design space and treat it as the main unit cell topology, disregarding unconnected material. FEA would be performed on this connected region and the material fraction constraint would be modified to apply to only the identified region. Connectivity between cells can be enforced with prescribed regions of solid and void material which are maintained throughout the iterative procedure. However, as illustrated in Figure 19, this limits the available design space and convergence to a minimum is more challenging. Ideally, a unit cell library with prescribed connectivity and optimized inner structures could be compiled, as proposed in the work by Hollister et al. [30].

The translation of theoretical optimal unit cells to CAD models for manufacturing can be eased by improving filtering. An appropriate filter will reduce checkerboard patterns and result in a design with a distinct boundary between solid and void regions. It was also shown by Sundararajan in 2010 that B-Spline based parametric smoothing functions are effective filters in topology optimization to control the size of the voids throughout the design domain, avoiding sharp changes in topology [84]. Furthermore, it is proposed by Sigmund et al. to perform a secondary shape optimization problem after topology optimization, with the optimal unit cell as an input. The shape optimization problem would smooth sharp corners in the optimal design, making manufacturing easier and eliminating stress concentrations [85].

There are many clinical considerations for the practical implementation of the proposed fracture fixation plate. The scope of this work is limited to two dimensions, so comparing the stiffness and material properties to a 3D plate is not valid. The thickness of the plate is an important contributing factor to stiffness, and bending and torsion should not be ignored. However, the benefit of designing with a cellular material is supported by showing an increase in the accessible design space, allowing for specific tailoring of mechanical and permeability properties. It is important to note that the optimal implant topology resulting from this procedure is highly sensitive to the applied loads during optimization, so a more realistic and complex loading scenario may improve implant design and performance.

Many fracture fixation plates are removed two years after being implanted. In this case, bone ingrowth into the plate is not desirable. A thin solid skin can therefore be designed around the scaffold so that it is shielded from the biological surfaces, preventing ingrowth. In the case of a permanent plate, the cellular design offers advantage in that fixation can be achieved through bone ingrowth into specific areas of the plate. However, the outer side of the permanent plate should also be covered with a solid skin so that the roughness of the microarchitecture does not irritate the soft tissue and cause further inflammation. The inner cellular structure is still beneficial in both permanent and non-permanent implants in that graded material properties can be achieved. This is especially advantageous in the design of a trabecular bone replacement, which would require a specific distribution of mechanical properties to match its non-homogeneity. Future trabecular bone applications of the methodology include the design of the stem of a hip or knee implant. These applications can suffer from stress-shielding induced failure, which is directly addressed by the proposed design.

5.3 Conclusion

In conclusion, cellular material provides a unique advantage in bone tissue scaffold design because material properties can be tailored to match non-homogeneous properties of bone. Inspired by the natural hierarchy of bone structure, a multi-scale designed scaffold can closely mimic the physiological and mechanical response of bone tissue. Hierarchical topology optimization can be used to design a scaffold with stiffness properties close to those of bone and high permeability for mass transport requirements. This was illustrated in a two-dimensional capacity through the design of a fracture fixation plate. The optimized cellular design can reduce stress shielding by tailoring mechanical properties to match bone, and reduce the occurrence of osteoporosis by minimizing disruption of blood flow. Future steps towards testing and manufacturing are discussed below. Addressing the identified limitations and next steps for the proposed methodology may allow for the introduction of hierarchically optimized bone tissue scaffold to the market.

5.4 Future work

Firstly, technical improvements including permeability calculations, filtering techniques, and imposing connectivity should all be addressed through the methods proposed in section 5.2. It is hypothesized that applying appropriate filtering at the unit cell level will reduce checkerboard patterns and a more distinct boundary between solid and void material will be produced. This will ease the translation of theoretical optimal unit cells to CAD models and reduce the discrepancy in performance shown in Table 13. Expansion of the proposed model into three dimensions will improve the clinical validity of the optimal results obtained, and more realistic loading and boundary conditions can be applied in the 3D design domain. The complex optimized topologies may have non-intuitive fracture and fatigue behaviour, as holes in the structure will act as stress concentrators [86]. Thus, a detailed stress analysis of all optimal designs is essential to ensure the mechanical performance is suitable for its application. Introducing a stress inequality constraint in the optimization statement may also improve the performance of the optimized designs (section 2.3.3). Samples of scaffold material should be built via additive manufacturing, such as electron beam melting, for *in vitro* and *in vivo* testing. Compliance with relevant ISO and FDA standards must be ensured throughout the design and testing procedure.

Appendices

Appendix A: Asymptotic homogenization

In general form, field variables in a unit cell can be approximated by:

$$u_i^n(x_i, y_i) = u_{0i}(x_i, y_i) + \eta u_{1i}(x_i, y_i) + \eta^2 u_{2i}(x_i, y_i) + \cdots, \qquad [31]$$

where u_i^n is the exact value of the field variable, u_{0i} is the macroscopic (average) value of the field variable (for example, continuum level displacements), u_{1i}, u_{2i}, etc. are perturbations in the field variables due to the microstructure (microstructural displacements), x_i are the global level coordinates, y_i are the micro level coordinates, and η is the ratio of the microstructure size to the total size of the analysis region (RVE). The two scales (macro and micro) are related by:

$$y_i = \frac{x_i}{\eta} \qquad [32]$$

Regular periodicity of a field variable of a heterogeneous medium is defined as having the following property:

$$\mathcal{F}(\boldsymbol{x} + \boldsymbol{NY}) = \mathcal{F}(\boldsymbol{x}) \qquad [33]$$

where $\boldsymbol{x}$ is a position vector (x_1, x_2, x_3) of a point, $\boldsymbol{N}$ is a 3 x 3 diagonal matrix:

$$\boldsymbol{N} = \begin{bmatrix} n_1 & 0 & 0 \\ 0 & n_2 & 0 \\ 0 & 0 & n_3 \end{bmatrix} \qquad [34]$$

with n_1, n_2 and n_3 as arbitrary integer numbers, and $\boldsymbol{Y}$ is a constant vector that describes the period of the structure. A cellular body with a periodic structure is shown in Figure 4. The function $\mathcal{F}$ of the position vector $\boldsymbol{x}$ can be scalar, vectorial, or tensorial. In the case of a composite material with repeating unit cell $\boldsymbol{Y}$, constitutional relations describe the mechanical behaviour in the form:

$$\sigma_{ij} = E_{ijkl}\varepsilon_{kl} \qquad [35]$$

where E_{ijkl} is a tensor, a periodic function of $\boldsymbol{x}$ **such as**:

$$E_{ijkl}(\boldsymbol{x} + \boldsymbol{NY}) = E_{ijkl}(\boldsymbol{x}) \qquad [36]$$

This can also be written as:

$$E_{ijkl}(x_1 + n_1 Y_1, x_2 + n_2 Y_2, x_3 + n_3 Y_3) = E_{ijkl}(x_1, x_2, x_3) \qquad [37]$$

Here, $E_{ijkl}(\boldsymbol{x})$ is $\boldsymbol{Y}$-periodic, and σ_{ij} and ε_{kl} are the stress and strain tensors respectively.
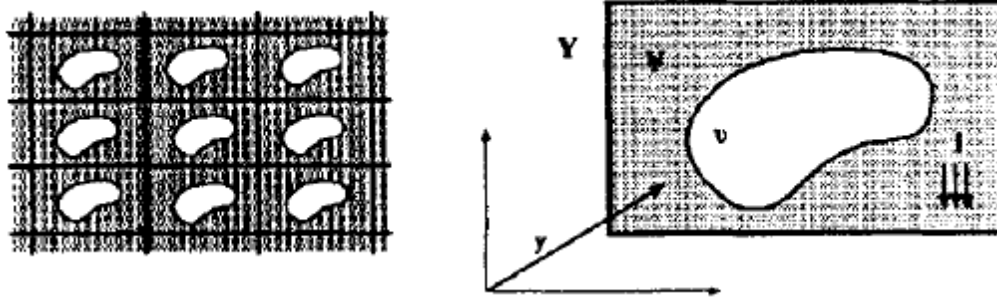
Figure 25: Cellular body with a periodic structure [40].

Equation [31] is substituted into the governing differential equations, and terms of the same order are separated and set equal to zero. The resulting equations govern the mechanical behaviour of the RVE at both the micro and macro levels. In general, the derivatives of any function $g^{\eta}(x) = g(x, y = x/\eta)$ with respect to x are written using the chain rule as follows:

$$\frac{\partial g^{\eta}}{\partial x_i} = \frac{\partial g}{\partial x_i} + \frac{1}{\eta}\frac{\partial g}{\partial y_i} \qquad [38]$$

Eq. [38] can be applied to the asymptotic expansion of the displacement u in Eq. [31] to obtain the small deformation strain tensor:

$$\varepsilon_{ij}(u) = \frac{1}{2}\left(\frac{\partial u_i^{\eta}}{\partial x_j} + \frac{\partial u_j^{\eta}}{\partial x_i}\right) \qquad [39]$$

$$= \frac{1}{2}\left[\left(\frac{\partial u_{0i}}{\partial x_j} + \frac{\partial u_{0j}}{\partial x_i}\right) + \left(\frac{\partial u_{1i}}{\partial y_j} + \frac{\partial u_{1j}}{\partial y_i}\right) + \eta\left(\frac{\partial u_{1i}}{\partial x_j} + \frac{\partial u_{1j}}{\partial x_i}\right)\right]$$

$$+ h.o.t.,$$

where h.o.t. denotes higher order terms and the other terms are as previously defined. The following strain tensors can be defined from [39] (neglecting terms of O(η) and higher).

$$\varepsilon_{ij} = \bar{\varepsilon}_{ij} + \varepsilon_{ij}^*, \quad \bar{\varepsilon}_{ij} = \frac{1}{2}\left(\frac{\partial u_{0i}}{\partial x_j} + \frac{\partial u_{0j}}{\partial x_i}\right), \qquad \varepsilon_{ij}^* = \frac{1}{2}\left(\frac{\partial u_{1i}}{\partial y_j} + \frac{\partial u_{1j}}{\partial y_i}\right), \qquad [40a\text{-}c]$$

where ε_{ij} is the micro strain tensor, $\bar{\varepsilon}_{ij}$ is the macro strain tensor and ε_{ij}^* is the fluctuating strain tensor. It is assumed that the fluctuating strain tensor varies periodically. The higher order terms can be neglected by assuming the material regime of interest be linear elastic. The virtual strain $\varepsilon_{ij}(v)$ is also expanded asymptotically as a function of x and y (where v is virtual displacement).

71

$$\varepsilon_{ij}(v) = \frac{1}{2}\left(\frac{\partial v_i^{\eta}}{\partial x_j} + \frac{\partial v_j^{\eta}}{\partial x_i}\right) \tag{41}$$

$$= \frac{1}{2}\left[\left(\frac{\partial v_{0i}}{\partial x_j} + \frac{\partial v_{0j}}{\partial x_i}\right) + \left(\frac{\partial v_{1i}}{\partial y_j} + \frac{\partial v_{1j}}{\partial y_i}\right) + \eta\left(\frac{\partial v_{1i}}{\partial x_j} + \frac{\partial v_{1j}}{\partial x_i}\right)\right]$$

$$+ h.o.t.,$$

Similarly to Eq. [40a-c], the following definitions of virtual strain components are made:

$$\varepsilon_{ij}(v) = \varepsilon_{ij}^0(v) + \varepsilon_{ij}^1(v), \quad \varepsilon_{ij}^0(v) = \frac{1}{2}\left(\frac{\partial v_{0i}}{\partial x_j} + \frac{\partial v_{0j}}{\partial x_i}\right), \tag{42a-c}$$

$$\varepsilon_{ij}^1(v) = \frac{1}{2}\left(\frac{\partial v_{1i}}{\partial y_j} + \frac{\partial v_{1j}}{\partial y_i}\right).$$

The standard weak form of the equilibrium equation is given by:

$$\int_{\Omega^{\eta}} C_{ijkl}\varepsilon_{ij}(v)\varepsilon_{kl}(u)d\Omega^{\eta} = \int_{\Gamma} t_i v_i d\Gamma \tag{43}$$

Where C_{ijkl} is the stiffness tensor, Ω^{η} represents the total macroscopic and microscopic domain of the composite material, and the tractions t_i (as well as any boundary displacements) are applied only to the macroscopic boundaries of the composite, not to any interior boundaries in the microstructure. The expanded forms of the strain tensor Equations [40a-c] and [42a-c] are substituted into Eq. [43] to obtain:

$$\int_{\Omega^{\eta}} C_{ijkl}(\varepsilon_{ij}^0(v) + \varepsilon_{ij}^1(v))(\bar{\varepsilon}_{kl} + \varepsilon_{kl}^*)d\Omega^{\eta} = \int_{\Gamma} t_i v_i d\Gamma \tag{44}$$

The function v can be chosen to vary only on the macroscopic or the microscopic level. If v varies only on the microscopic level and is constant on the macroscopic level (i.e. $\varepsilon_{ij}^0(\boldsymbol{v})$=0), then the microscopic equilibrium equation is obtained as:

$$\int_{\Omega^{\eta}} C_{ijkl}\varepsilon_{ij}^1(v)(\bar{\varepsilon}_{kl} + \varepsilon_{kl}^*)d\Omega^{\eta} = 0 \tag{45a}$$

Similarly, if v is chosen to only vary on the macroscopic level and is constant on the microscopic level (i.e. $\varepsilon_{ij}^1(\boldsymbol{v}) = 0$) the macroscopic equilibrium equation is obtained:

$$\int_{\Omega^\eta} C_{ijkl}\varepsilon_{ij}^0(v)(\bar{\varepsilon}_{kl} + \varepsilon_{kl}^*)d\Omega^\eta = \int_\Gamma t_i v_i d\Gamma \qquad \text{[45b]}$$

Since ε_{kl}^* varies periodically, [45a] and [45b] can be rewritten assuming η in the limit goes to zero as:

$$\int_\Omega \frac{1}{|V_{RVE}|} \int_{V_{RVE}} C_{ijkl}\varepsilon_{ij}^1(v)(\bar{\varepsilon}_{kl} + \varepsilon_{kl}^*)dV_{RVE}d\Omega = 0 \qquad \text{[46a]}$$

$$\int_\Omega \frac{1}{|V_{RVE}|} \int_{V_{RVE}} C_{ijkl}\varepsilon_{ij}^0(v)(\bar{\varepsilon}_{kl} + \varepsilon_{kl}^*)dV_{RVE}d\Omega = \int_\Gamma t_i v_i d\Gamma \qquad \text{[46b]}$$

Eq. [46a] will be satisfied if the integral over the RVE is zero, so [46a] can be rewritten as:

$$\int_{V_{RVE}} C_{ijkl}\varepsilon_{ij}^1(v)\varepsilon_{kl}^* dV_{RVE} = -\int_{V_{RVE}} C_{ijkl}\varepsilon_{ij}^1(v)\bar{\varepsilon}_{kl} dV_{RVE} \qquad \text{[47]}$$

Any arbitrary $\bar{\varepsilon}_{kl}$ is written as a linear combination of unit strains. Assuming that the base material of the lattice material is linearly elastic, these unit strain cases are applied and combined to determine the overall behaviour of the RVE. In 2D, the 4 unit strain cases are written as:

$$\bar{\varepsilon}_{pm}^{11} = -\begin{bmatrix} 1 & 0 \\ 0 & 0 \end{bmatrix}, \bar{\varepsilon}_{pm}^{22} = -\begin{bmatrix} 1 & 0 \\ 0 & 0 \end{bmatrix}, \bar{\varepsilon}_{pm}^{12} = -\begin{bmatrix} 1 & 0 \\ 0 & 0 \end{bmatrix}, \bar{\varepsilon}_{pm}^{21} = -\begin{bmatrix} 1 & 0 \\ 0 & 0 \end{bmatrix}.$$

These unit strain cases are substituted into the right hand side of [47] to then obtain a stress tensor from:

$$\sigma_{ij}^{*kl} = C_{ijpm}\bar{\varepsilon}_{pm}^{kl} \qquad \text{[48]}$$

An auxiliary equation to solve for ε_{pm}^* in [47] using [48] is:

$$\int_{V_{RVE}} C_{ijkl}\varepsilon_{ij}^1(v)\varepsilon_{ij}^{*kl}(u)dV_{RVE} = \int_{V_{RVE}} \varepsilon_{ij}^1(v)\sigma_{ij}^{*kl}dV_{RVE} \qquad \text{[49]}$$

The periodic boundary condition is applied to the strain field ε_{ij}^{*kl} by ensuring that the displacements at opposite sides of the RVE are equal. Once ε_{ij}^{*kl} is determined, the solution to [47] is recovered by:

$$\varepsilon_{ij}^* = -\varepsilon_{ij}^{*kl}\bar{\varepsilon}_{kl} \qquad \text{[50]}$$

Recalling Eq. [42a-c], the relationship between the local RVE strain and the average strain may be written using the local structure tensor as:

$$\varepsilon_{ij} = M_{ijkl}\bar{\varepsilon}_{kl}, \quad M_{ijkl} = \frac{1}{2}\left(\delta_{ik}\delta_{jl} + \delta_{il}\delta_{jk}\right) - \varepsilon_{ij}^{*kl} \qquad \text{[51a,b]}$$

where δ is the Kronecker delta. The relationship between the local strain and the average strain [51a,b] is then substituted into the macroscopic level equilibrium equations:

$$\int_{\Omega} \frac{1}{|V_{RVE}|} \int_{V_{RVE}} C_{ijkl}M_{klpm}dV_{RVE}\,\varepsilon_{ij}^0(v)\bar{\varepsilon}_{pm}d\Omega = \int_{\Gamma} t_i v_i d\Gamma \qquad \text{[52]}$$

where $\bar{\varepsilon}_{pm}$ and $\varepsilon_{ij}^0(\boldsymbol{v})$ are outside the integral over the RVE since they have constant values over the RVE. Finally, the homogenized stiffness tensor is formulated as:

$$\boldsymbol{C}^H = \bar{C}_{ijkl} = \frac{1}{|V_{RVE}|} \int_{V_{RVE}} C_{ijpm}M_{pmkl}dV_{RVE} \qquad \text{[53]}$$

Appendix B: Standard mechanics homogenization

The standard mechanics approach is a mathematically simpler alternative to asymptotic homogenization for determining effective stiffness of a cellular material. The boundary conditions are specifically chosen so that an average strain (if displacement BC) or average stress (if traction BC) is produced within a homogeneous material with the size of the RVE. It is important to note that $\bar{C}_{ijkl}$ calculated here is dependent on the RVE size, unlike asymptotic homogenization where $\bar{C}_{ijkl}$ is independent due to the periodicity assumption used in determining M_{ijkl}.

A displacement based finite element formulation was used by Hassani et al. to compare homogenization and standard mechanics analyses for period porous composites [40]. It was found that for one dimensional analysis of composite bars, the two methods are equivalent. Analysis of two and three dimensional periodic structures yield differences between the two methods, standard mechanics is based solely on applied boundary conditions, whereby local stress and strain state are not fully captured. It is suggested that the asymptotic homogenization theory is superior to the standard mechanics method.

The following expression, based on the divergence theorem, relates the average strain and the displacement BCs:

$$\bar{\varepsilon}_{ij} = \frac{1}{|V_{RVE}|} \int_{V_{RVE}} \varepsilon_{ij}\, dV_{RVE} = \frac{1}{|V_{RVE}|} \int_{S_{RVE}} \frac{1}{2}(u_i n_j + u_j n_i)\, dS_{RVE}$$

[54]

Here, $\bar{\varepsilon}_{ij}$ is average strain, ε_{ij} is local strain in the RVE, u_i is the displacement imposed on the RVE boundary, n_i is the normal vector to the RVE boundary, and S_{RVE} is the RVE boundary. Generally, the actual local boundary conditions are not known, and as such, the displacements are chosen to be uniform. The standard weak form of the equilibrium equations is then solved to calculate the local RVE strain. For the case of applied boundary displacements, the weak form of the RVE equilibrium equations is:

$$\int_{V_{RVE}} C_{ijkl}\varepsilon_{ij}(v)\varepsilon_{mn}^{kl}(u)\, dV_{RVE} = \int_{S_{RVE}} \lambda v_i\left(u_i^{kl} - g_i^{kl}\right)\, dS_{RVE}$$

[55]

The variables used above are defined as follows: C_{ijkl} is the stiffness tensor of the RVE, $\varepsilon_{ij}(v)$ is the virtual strain, $\varepsilon_{mn}^{kl}(u)$ is the total microstructural strain (for the klth displacement), λ is a penalty factor, where displacements are implemented using a penalty method, v_i is the virtual displacement, u_i^{kl} is the boundary displacement, and g_i^{kl} is the specified displacement that would produce a uniform average strain $\bar{\varepsilon}_{kl}$ in a and the local structure tensor M_{ijpm} can then be calculated to relate the average strain $\bar{\varepsilon}_{pm}^{kl}$ to the local strain ε_{ij}^{kl}:

$$\varepsilon_{ij}^{kl} = M_{ijpm}\bar{\varepsilon}_{pm}^{kl}$$

[56]

With M_{ijpm} determined, the local strain at any point in the RVE can be calculated from an arbitrary applied strain using:

$$\varepsilon_{ij} = M_{ijkl}\bar{\varepsilon}_{kl}$$

[57]

The effective stiffness tensor $\bar{C}_{ijkl}$ can also be calculated. $\bar{C}_{ijkl}$ relates the average strain to the average stress:

$$\bar{\sigma}_{ij} = \bar{C}_{ijkl}\bar{\varepsilon}_{kl}$$

[58]

Using Hooke's Law at the microscopic level, $\sigma_{ij} = C_{ijkl}\varepsilon_{kl}$, we can integrate both sides of the equation above:

$$\frac{1}{|V_{RVE}|} \int\limits_{V_{RVE}} \sigma_{ij} dV_{RVE} = \frac{1}{|V_{RVE}|} \int\limits_{V_{RVE}} C_{ijkl}\varepsilon_{kl} dV_{RVE} \qquad [59]$$

Substituting the relations for average stress and strain, and equation [23] gives:

$$\overline{\sigma}_{ij} = \frac{1}{|V_{RVE}|} \int\limits_{V_{RVE}} C_{ijpm} M_{pmkl} dV_{RVE}\overline{\varepsilon}_{kl} \qquad [60]$$

Finally, the effective stiffness tensor can be defined as:

$$\overline{C}_{ijkl} = \frac{1}{|V_{RVE}|} \int\limits_{V_{RVE}} C_{ijpm} M_{pmkl} dV_{RVE} \qquad [61]$$

Appendix C: Optimality criteria sensitivity calculation

Implementing the optimality criteria method for a minimum compliance problem requires computing the sensitivity of the objective function. This procedure involves writing the FEM form of the minimum compliance problem:

$$\min_{u,\rho_e} f^T u \qquad [62]$$

$$s.t. \ \left(\sum_{e=1}^{N} \rho_e^p K_e \right) u = f$$

$$\sum_{e=1}^{N} v_e \rho_e \leq V, \qquad 0 < \rho_{min} \leq \rho_e \leq 1, \qquad e = 1, ..., N$$

Rewriting this as a problem in the design variables only results in:

$$\min_{\rho_e} c(\rho_e) \qquad [63]$$

$$s.t. \ \sum_{e=1}^{N} v_e \rho_e \leq V, \qquad 0 < \rho_{min} \leq \rho_e \leq 1, \qquad e = 1, ..., N$$

where $c(\rho_e)$ is compliance. Here, the equilibrium constraint is considered part of the FEM function:

$$c(\rho_e) = f^T u, \qquad where \ u \ solves \qquad \sum_{e=1}^{N} \rho_e^p K_e u = f \qquad [64]$$

The optimization algorithm requires gradients only in relative density, which can easily be derived from the above equation. The adjoint method is used to calculate the derivative, beginning by adding the zero function:

$$c(\rho) = f^T u - \tilde{u}^T(Ku - f) \tag{65}$$

where $\tilde{u}$ is an arbitrary fixed vector. Using this equation the gradient of compliance is obtained as:

$$\frac{\partial c}{\partial \rho_e} = (f^T - \tilde{u}^T K)\frac{\partial u}{\partial \rho_e} - \tilde{u}^T \frac{\partial K}{\partial \rho_e} u$$

$$\frac{\partial c}{\partial \rho_e} = -\tilde{u}^T \frac{\partial K}{\partial \rho_e} u \tag{66}$$

where $\tilde{u}$ satisfies the adjoint equation $f^T - \tilde{u}^T K = 0$. For compliance, we see in this case that $\tilde{u} = u$, and the compliance gradient can be written simply as:

$$\frac{\partial c}{\partial \rho_e} = -p\rho_e^{p-1}u^T K_e u \tag{67}$$

This formulation makes derivatives of the compliance problem straightforward to calculate.

Appendix D: Methods of comparing matrices for target matching

To minimize the difference between two matrices, it is necessary to find an appropriate representation of each matrix for comparison. There are various methods for representing a matrix, several of which are described below.

Matrix norm

The norm of a tensor can be calculated and used for comparison with another tensor. A norm to a matrix is what the absolute value is to a real number, and can be defined in various ways. For example, the Euclidean norm (2-norm, or spectral norm) is the square root of the largest non-negative eigenvalue λ_i of the positive-semidefinite product of the matrix by its transpose (AAT). A is a n x n square matrix.

$$\|A\|_E = \max_i\{\sqrt{\lambda_i}\} \tag{68}$$

Note that positive semi-definite means that for matrix A, the following must be true for all x in Rn, where x* is the conjugate transpose of x:

$$x^*Ax \geq 0 \tag{69}$$

The Frobenius norm is the square root of the sum of the squares of the entries of the matrix:

$$\|\boldsymbol{A}\|_F = \sqrt{\sum_{j=1}^{n}\sum_{i=1}^{n} a_{ij}^2}$$

[70]

The Chebyshev norm or infinity norm is the maximum absolute value of the entries of the matrix:

$$\|\boldsymbol{A}\|_\infty = \max_{i,j}\{|a_{ij}|\}$$

[71]

The p-norm is defined as the following:

$$\|\boldsymbol{A}\|_p = \left(\sum_{j=1}^{n}\sum_{i=1}^{n}|a_{ij}|^p\right)^{\frac{1}{p}}$$

[72]

Sum of components

A tensor can be represented as a single number, which is a weighted sum of all or some of its components. The procedure described by Lin et al. (2003) target matches the 3D stiffness matrix with six orthotropic elastic properties (three Young's moduli and three shear moduli). In 2D, the plane stress stiffness matrix is represented as:

$$C = \frac{E}{1-v^2}\begin{bmatrix} 1 & v & 0 \\ v & 1 & 0 \\ 0 & 0 & 1-v \end{bmatrix}$$

[73]

In this study, the difference in target and effective stiffness matrices is represented as a weighted sum of the difference in two Young's moduli and one shear moduli:

$$\min_{\rho}\left(\left|\frac{C_{11}^{H}-C_{11}^{*}}{C_{11}}\right|_{L_2} + \left|\frac{C_{22}^{H}-C_{22}^{*}}{C_{22}}\right|_{L_2} + \left|\frac{C_{33}^{H}-C_{33}^{*}}{C_{33}}\right|_{L_2}\right)$$

[74]

where ρ is the design variable, relative density, superscript H represents effective property and superscript * represents target property. The L_2 norm (or Euclidean norm) operator is defined above. Each component is normalized with base material properties.

Condition number

The condition number is a property of a matrix that indicates the sensitivity of the solution of a linear equation to errors in the data. For example, in the linear equation Ax = b, the condition number of A gives an upper bound on the inaccuracy of x. The condition number κ of a target matrix is a unique property of that matrix and all of its multiples, because it is calculated based on the matrix norm.

78

In the linear equation Ku=f, where K is stiffness, u is displacement and f is force, the condition number of the stiffness matrix would give an indication of inaccuracy in displacement as a result of variability in force measurement. A large condition number indicates that a small error in f may cause a large error in u, and a small condition number indicates that error in u will not be significantly larger than error in f.

In the case of a square matrix, error in K-1f is K-1e, where e is error in f. The condition number is calculated as the maximum ratio of relative error in u (the solution) divided by relative error in f:

$$\frac{\|K^{-1}e\| \, / \, \|K^{-1}f\|}{\|e\| \, / \, \|f\|} \tag{75}$$

This is equal to:

$$(\|K^{-1}e\| \, / \, \|e\|) \cdot (\|f\| \, / \, \|K^{-1}f\|) \tag{76}$$

The maximum value of the equation above (with nonzero f and e) is the product of the two operator norms (any consistent norm, where $\kappa(K) \geq 1$):

$$\kappa(K) = \|K^{-1}\| \cdot \|K\| \tag{77}$$

This method of comparing matrices using condition number maybe unreliable because the condition number of the effective stiffness matrix may be the same as the target, but the stiffness matrix could be any multiple of the target.

Bulk Modulus

For the case of isotropic linear elastic materials, there are a variety of properties other than the stiffness matrix than can be compared to achieve a target material. For example, Kang et al (2010) compare bulk modulus, K for the purpose of topology optimization with target matching $(K^H - K^*)$. If the design is constrained to be isotropic, bulk modulus can be calculated based on homogenized E and v (Young's modulus and Poisson's ratio, respectively) and used for target matching:
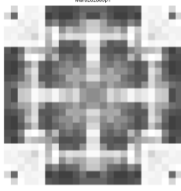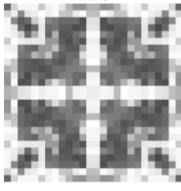
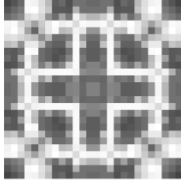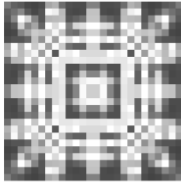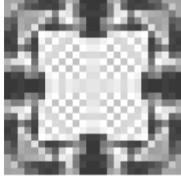$$K = \frac{E}{3(1 - 2v)} \tag{78}$$

Appendix E: Optimal topologies - fracture fixation plate

Table 14: Optimal fracture fixation plates with varying material fraction and penalty factor.

Material fraction, V^* (%)	Penalty factor, p	Optimal topology
40	1	
40	1.1	
40	1.25	
40	3	
55	1	
55	1.1	
55	1.25	
55	3	
60	1	
60	1.1	
60	1.25	
60	3	

Appendix F: Optimal topologies - unit cells

Table 15: Optimal unit cell topologies with target stiffness determined by relative density of 60%. Mesh size 26 x 26.

	Porosity	P	Stiffness % Difference			Permeability % Difference
	64.86	1	-9.30 7.40 0	7.40 -9.30 0	0 0 6.59	0.254
	65.23	1	-5.52 4.80 0	4.80 -5.52 0	0 0 2.14	-0.447
	65.14	1	-6.43 5.27 0	5.27 -6.437 0	0 0 0.95	-0.265
	64.34	1.5	-13.52 -3.61 0	-3.61 -13.52 0	0 0 0.32	1.191
	65.77	1.5	-10.98 5.16 0	5.16 -10.98 0	0 0 2.92	-1.417
	65.15	1.5	-12.78 -0.01 0	-0.01 -12.78 -100	0 0 6.72	-0.298
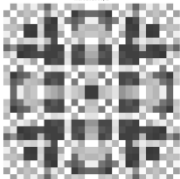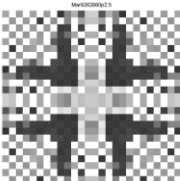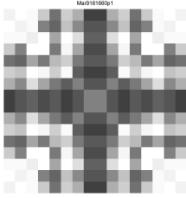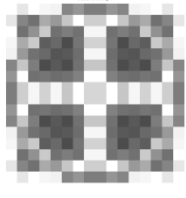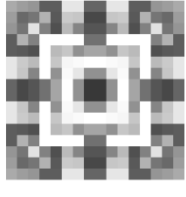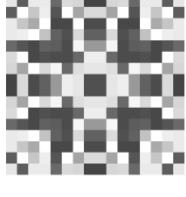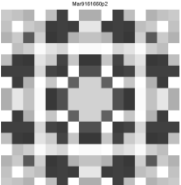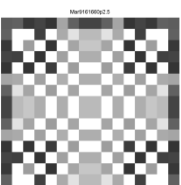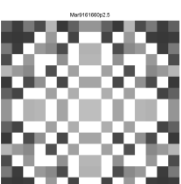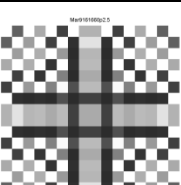
			Matrix			
	65.49	2	-15.08	-4.83	0	-0.900
			-4.83	-15.08	0	
			0	0	-6.50	
	65.79	2	-13.37	-4.13	0	-1.451
			-4.13	-13.37	0	
			0	0	-5.21	
	65.50	2	-13.72	-3.87	0	-0.910
			-3.87	-13.72	0	
			0	0	-6.53	
	65.87	2.5	-16.61	-10.77	0	-1.571
			-10.77	-16.61	0	
			0	0	-10.58	
	66.95	2.5	-13.17	-10.22	0	-3.463
			-10.22	-13.17	0	
			0	0	-8.60	
	65.13	2.5	-17.83	-12.74	0	-0.248
			-12.74	-17.83	0	
			0	0	-10.90	

Table 16: Optimal unit cell topologies with target stiffness determined by relative density of 60 %. Mesh size 16 x 16.

	Porosity	P	Stiffness % Difference			Permeability % Difference
	65.27	1	-14.81	5.46	0	-0.530
			5.46	-14.81	0	
			0	0	11.12	
	66.26	1	-5.28	5.22	0	-2.350
			5.22	-5.28	0	
			0	0	2.52	
	65.64	1	-9.72	7.33	0	-1.244
			7.33	-9.72	0	
			0	0	5.55	
	66.66	1.5	-8.68	6.52	0	-2.992
			6.52	-8.68	0	
			0	0	4.30	
	64.85	1.5	-11.11	3.90	0	0.197
			3.90	-11.11	0	
			0	0	2.73	
	65.08	1.5	-6.92	1.11	0	-0.192
			1.11	-6.92	0	
			0	0	0.90	

	64.60	2	-10.16	-6.18	0	0.678
			-6.18	-10.16	0	
			0	0	-3.94	
	64.97	2	-7.80	5.25	0	-0.072
			5.256	-7.80	0	
			0	0	6.04	
	65.79	2	-7.43	-1.44	0	-1.434
			-1.44	-7.43	0	
			0	0	-1.56	
	67.54	2.5	-11.06	-9.54	0	-4.476
			-9.54	-11.06	0	
			0	0	-7.35	
	66.22	2.5	-15.20	-13.45	0	-2.192
			-13.45	-15.20	0	
			0	0	-13.63	
	64.01	2.5	-17.82	-17.08	0	1.651
			-17.08	-17.82	0	
			0	0	-13.56	

Appendix G: Objective function comparison – sample calculation

In general, the objective function for each unit cell is evaluated as:

$$f(x) = w_1 \left\| C^H - C^* \right\|_{L_2} + w_2 \left(\frac{P^H}{P^*} - 1 \right)^2$$

$$f(x) = w_1 \left[\left(\frac{C_{11}^H}{C_{11}^*} - 1 \right) + \left(\frac{C_{22}^H}{C_{22}^*} - 1 \right) + \left(\frac{C_{12}^H}{C_{12}^*} - 1 \right) \right] + w_2 \left(\frac{P^H}{P^*} - 1 \right)^2$$

where $w_1 = w_2 = 0.5$ in the case shown in section 4.4. The homogenized (effective) stiffness C^H and the target stiffness C^* are 3x3 matrices. P^H is effective permeability and P^* is target permeability.

The objective function is evaluated iteratively via scripts written MATLAB. For Unit Cell 2 in Table 13, the final value of the objective function is calculated as follows:

$$f(x)^{optimal} = 0.5 * \left[\left(\frac{0.2599}{0.2374} - 1 \right) + \left(\frac{0.2599}{0.2374} - 1 \right) + \left(\frac{0.0668}{0.0712} - 1 \right) \right] + w_2 \left(\frac{0.6127}{0.5944} - 1 \right)^2$$

$$f(x)^{optimal} = 0.0786$$

The interpreted CAD model of Unit Cell 2 was meshed in ANSYS and the effective properties were determined. The objective function was calculated in the same way:

$$f(x)^{CAD} = 0.5 * \left[\left(\frac{0.2075}{0.2374} - 1 \right) + \left(\frac{0.2075}{0.2374} - 1 \right) + \left(\frac{0.0197}{0.0712} - 1 \right) \right] + w_2 \left(\frac{0.5666}{0.5944} - 1 \right)^2$$

$$f(x)^{CAD} = 0.1864$$

To compare the CAD model to the original optimal unit cell, the percent difference of their objective function values is found as follows:

$$\left(1 - \frac{f(x)^{optimal}}{f(x)^{CAD}} \right) * 100\% = \left(1 - \frac{0.0786}{0.1864} \right) * 100\% = 57.83\%$$

References

[1]   V. I. Sikavitsas, J. S. Temenoff, and A. G. Mikos, "Biomaterials and bone mechanotransduction," *Biomaterials,* vol. 22, pp. 2581-93, Oct 2001.

[2]   J. S. Khurana. (2009). *Bone pathology*. Available: http://dx.doi.org/10.1007/978-1-59745-347-9

[3]   S. v. Gaalen, M. Kruyt, G. Meijer, A. Mistry, A. Mikos, J. v. d. Beucken*, et al.*, "Chapter 19 - Tissue engineering of bone," in *Tissue Engineering*, C. v. Blitterswijk, P. Thomsen, A. Lindahl, J. Hubbell, D. F. Williams, R. Cancedda*, et al.*, Eds., ed Burlington: Academic Press, 2008, pp. 559-610.

[4]   M. F. A. Lorna J. Gibson, *Cellular solids: Structure and Properties*. Cambridge; New York: Cambridge University Press, 1997.

[5]   M. F. A. L.J. Gibson, B.A. Harley, *Cellular Materials in Nature and Medicine*. Cambridge, U.K.: Cambridge University Press, 2010.

[6]   L. G. Cox, B. van Rietbergen, C. C. van Donkelaar, and K. Ito, "Analysis of bone architecture sensitivity for changes in mechanical loading, cellular activity, mechanotransduction, and tissue properties," *Biomech Model Mechanobiol,* vol. 10, pp. 701-12, Oct 2011.

[7]   S. C. Cowin, "The significance of bone microstructure in mechanotransduction," *J Biomech,* vol. 40 Suppl 1, pp. S105-9, 2007.

[8]   K. Kapinas and A. M. Delany, "MicroRNA biogenesis and regulation of bone remodeling," *Arthritis Res Ther,* vol. 13, p. 220, 2011.

[9]   DoITPoMS. (2013, February). *Structure and Composition of Bone*. Available: http://www.doitpoms.ac.uk/tlplib/bones/structure.php

[10]   I. Parkinson and N. Fazzalari, "Characterisation of Trabecular Bone Structure," in *Skeletal Aging and Osteoporosis*. vol. 5, M. J. Silva, Ed., ed: Springer Berlin Heidelberg, 2013, pp. 31-51.

[11]   J. O. Hollinger, *Bone tissue engineering*. Boca Raton: CRC Press, 2005.

[12]   Y. H. Chen, J. Cadman, and Q. Li, "Effect of scaffold architecture on tissue regeneration," in *6th World Congress of Biomechanics, WCB 2010 - In Conjunction with 14th International Conference on Biomedical Engineering, ICBME and 5th Asia Pacific Conference on Biomechanics, APBiomech, August 1, 2010 - August 6, 2010*, Singapore, Singapore, 2010, pp. 815-818.

[13]   S. J. Hollister, "Porous scaffold design for tissue engineering," *Nature Materials,* vol. 4, pp. 518-24, 07/ 2005.

[14]   C. Y. Lin, N. Kikuchi, and S. J. Hollister, "A novel method for biomaterial scaffold internal architecture design to match bone elastic properties with desired porosity," *J Biomech,* vol. 37, pp. 623-36, May 2004.

[15]   M. A. Woodruff, C. Lange, J. Reichert, A. Berner, F. Chen, P. Fratzl*, et al.*, "Bone tissue engineering: From bench to bedside," *Materials Today,* vol. 15, pp. 430-435, 2012.

[16]   S. A. Khanoki and D. Pasini, "The fatigue design of a bone preserving hip implant with functionally graded cellular material," *Journal of Medical Devices, Transactions of the ASME,* vol. 7, 2013.

[17]   S. Arabnejad Khanoki and D. Pasini, "Fatigue design of a mechanically biocompatible lattice for a proof-of-concept femoral stem," *Journal of the Mechanical Behavior of Biomedical Materials,* vol. 22, pp. 65-83, 2013.

[18]   E. Masoumi Khalil Abad, S. Arabnejad Khanoki, and D. Pasini, "Fatigue design of lattice materials via computational mechanics: Application to lattices with smooth transitions in cell geometry," *International Journal of Fatigue,* vol. 47, pp. 126-136, 2013.

[19]   S. A. Khanoki and D. Pasini, "Multiscale design and multiobjective optimization of orthopaedic cellular hip implants," in *ASME 2011 International Design Engineering Technical Conferences and Computers and Information in Engineering Conference, IDETC/CIE 2011, August 28, 2011 - August 31, 2011*, Washington, DC, United states, 2011, pp. 935-944.

[20] S. Arabnejad Khanoki and D. Pasini, "Multiscale design and multiobjective optimization of orthopedic hip implants with functionally graded cellular material," *Journal of Biomechanical Engineering,* vol. 134, 2012.

[21] E. M. K. Abad, S. A. Khanoki, and D. Pasini, "Shape design of periodic cellular materials under cyclic loading," in *ASME 2011 International Design Engineering Technical Conferences and Computers and Information in Engineering Conference, IDETC/CIE 2011, August 28, 2011 - August 31, 2011*, Washington, DC, United states, 2011, pp. 945-954.

[22] S. J. Hollister, "Scaffold design and manufacturing: From concept to clinic," *Advanced Materials,* vol. 21, pp. 3330-3342, 2009.

[23] S. J. Hollister and W. L. Murphy, "Scaffold translation: Barriers between concept and clinic," *Tissue Engineering - Part B: Reviews,* vol. 17, pp. 459-474, 2011.

[24] Y. Chen, M. Schellekens, S. Zhou, J. Cadman, W. Li, R. Appleyard*, et al.*, "Design optimization of scaffold microstructures using wall shear stress criterion towards regulated flow-induced erosion," *J Biomech Eng,* vol. 133, p. 081008, Aug 2011.

[25] S. J. Hollister, R. D. Maddox, and J. M. Taboas, "Optimal design and fabrication of scaffolds to mimic tissue properties and satisfy biological constraints," *Biomaterials,* vol. 23, pp. 4095-103, Oct 2002.

[26] E. A. Sander and E. A. Nauman, "Permeability of musculoskeletal tissues and scaffolding materials: experimental results and theoretical predictions," *Critical Reviews in Biomedical Engineering,* vol. 31, pp. 1-26, / 2003.

[27] J. C. Utting, S. P. Robins, A. Brandao-Burch, I. R. Orriss, J. Behar, and T. R. Arnett, "Hypoxia inhibits the growth, differentiation and bone-forming capacity of rat osteoblasts," *Experimental Cell Research,* vol. 312, pp. 1693-1702, 6/10/ 2006.

[28] Y. Chen, S. Zhou, J. Cadman, and Q. Li, "Design of cellular porous biomaterials for wall shear stress criterion," *Biotechnol Bioeng,* vol. 107, pp. 737-46, Nov 1 2010.

[29] P. Habibovic, H. Yuan, C. M. van der Valk, G. Meijer, C. A. van Blitterswijk, and K. de Groot, "3D microenvironment as essential element for osteoinduction by biomaterials," *Biomaterials,* vol. 26, pp. 3565-75, Jun 2005.

[30] S. J. Hollister and C. Y. Lin, "Computational design of tissue engineering scaffolds," *Computer Methods in Applied Mechanics and Engineering,* vol. 196, pp. 2991-2998, 2007.

[31] J. Knychala, N. Bouropoulos, C. J. Catt, O. L. Katsamenis, C. P. Please, and B. G. Sengers, "Pore geometry regulates early stage human bone marrow cell tissue formation and organisation," *Ann Biomed Eng,* vol. 41, pp. 917-30, May 2013.

[32] S. Van Bael, Y. C. Chai, S. Truscello, M. Moesen, G. Kerckhofs, H. Van Oosterwyck*, et al.*, "The effect of pore geometry on the in vitro biological behavior of human periosteum-derived cells seeded on selective laser-melted Ti6Al4V bone scaffolds," *Acta Biomater,* vol. 8, pp. 2824-34, Jul 2012.

[33] H. Kang, C.-Y. Lin, and S. J. Hollister, "Topology optimization of three dimensional tissue engineering scaffold architectures for prescribed bulk modulus and diffusivity," *Structural and Multidisciplinary Optimization,* vol. 42, pp. 633-644, 2010.

[34] E. K. Tacvorian, "Evaluation of Canine Fracture Fixation Bone Plates," Degree of Master of Science, Biomedical Engineering, Worchester Polytechnic Institute, 2012.

[35] T. Dwyer. (2009). *The Bone School*. Available: http://www.boneschool.com/trauma/principles-internal-fixation

[36] H. Fouad, "Effects of the bone-plate material and the presence of a gap between the fractured bone and plate on the predicted stresses at the fractured bone," *Medical Engineering & Physics,* vol. 32, pp. 783-9, 2010.

[37] V. K. Ganesh, K. Ramakrishna, and D. Ghista, "Biomechanics of bone-fracture fixation by stiffness-graded plates in comparison with stainless-steel plates," *BioMedical Engineering OnLine,* vol. 4, pp. 1-15, 2005/07/27 2005.

[38]	K. K. S. M. Perren, O. Pohler, M. Predieri, S. Steinemann, and E. Gautier, "The limited contact dynamic compression plate (LC-DCP) " *Arch Orthop Trauma Surg,* vol. 109, 1990.

[39]	P. G. Coelho, P. R. Fernandes, J. M. Guedes, and H. C. Rodrigues, "A hierarchical model for concurrent material and topology optimisation of three-dimensional structures," *Structural and Multidisciplinary Optimization,* vol. 35, pp. 107-115, 2007.

[40]	B. Hassani, "A direct method to derive the boundary conditions of the homogenization equation for symmetric cells," *Communications in Numerical Methods in Engineering,* vol. 12, pp. 185-196, 1996.

[41]	M. S. A. Elsayed and D. Pasini, "Analysis of the elastostatic specific stiffness of 2D stretching-dominated lattice materials," *Mechanics of Materials,* vol. 42, pp. 709-725, 2010.

[42]	M. S. A. Elsayed and D. Pasini, "Characterization and performance optimization of 2D lattice materials with hexagonal Bravais lattice symmetry," in *2009 ASME International Design Engineering Technical Conferences and Computers and Information in Engineering Conference, DETC2009, August 30, 2009 - September 2, 2009*, San Diego, CA, United states, 2010, pp. 1315-1323.

[43]	M. S. A. Elsayed and D. Pasini, "Multiscale model of the effective properties of the octet-truss lattice material," in *12th AIAA/ISSMO Multidisciplinary Analysis and Optimization Conference, MAO, September 10, 2008 - September 12, 2008*, Victoria, BC, Canada, 2008.

[44]	M. S. A. Elsayed and D. Pasini, "Multiscale structural design of columns made of regular octet-truss lattice material," *International Journal of Solids and Structures,* vol. 47, pp. 1764-1774, 2010.

[45]	M. S. A. Elsayed, H. Clement, and D. Pasini, "Structural analysis of pin jointed lattice structures," in *3rd International Conference on Advances and Trends in Engineering Materials and their Applications, AES-ATEMA'2009, July 6, 2009 - July 10, 2009*, Montreal, QC, Canada, 2009, pp. 51-57.

[46]	M. S. A. Elsayed and D. Pasini, "Theoretical and experimental characterization of the 34.6 2D lattice material," in *ASME 2010 International Design Engineering Technical Conferences and Computers and Information in Engineering Conference, IDETC/CIE2010, August 15, 2010 - August 18, 2010*, Montreal, QC, Canada, 2010, pp. 11-20.

[47]	A. Vigliotti and D. Pasini, "Linear multiscale analysis and finite element validation of stretching and bending dominated lattice materials," *Mechanics of Materials,* vol. 46, pp. 57-68, 2012.

[48]	A. Vigliotti, V. S. Deshpande, and D. Pasini, "Non linear constitutive models for lattice materials," *Journal of the Mechanics and Physics of Solids,* vol. 64, pp. 44-60, 2014.

[49]	A. Vigliotti and D. Pasini, "Stiffness and strength of tridimensional periodic lattices," *Computer Methods in Applied Mechanics and Engineering,* vol. 229-232, pp. 27-43, 2012.

[50]	S. J. Hollister and N. Kikuchi, "Comparison of homogenization and standard mechanics analyses for periodic porous composites," *Computational Mechanics,* vol. 10, pp. 73-95, 1992.

[51]	S. Arabnejad and D. Pasini, "Mechanical properties of lattice materials via asymptotic homogenization and comparison with alternative homogenization methods," *International Journal of Mechanical Sciences,* vol. 77, pp. 249-262, 2013.

[52]	E. Sanchez-Palencia, *Non-homogeneous media and vibration theory*. Berlin, West Germany: Springer-Verlag, 1980.

[53]	J. K. Guest and J. H. Prévost, "Optimizing multifunctional materials: Design of microstructures for maximized stiffness and fluid permeability," *International Journal of Solids and Structures,* vol. 43, pp. 7028-7047, 2006.

[54]	P. A. a. B. R. L. Sinh Trinh, "Effective Diffusivities of Point-Like Molecules in Isotropic Porous Media by Monte Carlo Simulation," *Transport in Porous Media,* vol. 38, pp. 241–259, 2000.

[55]	H. L. Weissberg, "Effective Diffusion Coefficient in Porous Media," *Journal of Applied Physics,* vol. 34, p. 2636, 1963.

[56]   P. J. Prendergast, R. Huiskes, and K. Søballe, "Biophysical stimuli on cells during tissue differentiation at implant interfaces," *Journal of Biomechanics,* vol. 30, pp. 539-548, 6// 1997.

[57]   J. E. Cadman, S. Zhou, Y. Chen, and Q. Li, "On design of multi-functional microstructural materials," *Journal of Materials Science,* vol. 48, pp. 51-66, 2013.

[58]   M. P. S. Bendsoe, Ole, "Topology Optimization: Theory, Methods, and Applications," ed: Springer-Verlag Berlin Heidelberg, 2003.

[59]   K. S. a. N. Kikuchi, "A homogenization method for shape and topologoy optimization," *Computer Methods in Applied Mechanics and Engineering,* vol. 93, pp. 291-318, 1991.

[60]   G. I. N. Rozvany, "Aims, scope, methods, history and unified terminology of computer-aided topology optimization in structural mechanics," *Structural and Multidisciplinary Optimization,* vol. 21, pp. 90-108, 2001/04/01 2001.

[61]   A. Rietz, "Sufficiency of a finite exponent in SIMP (power law) methods," *Structural and Multidisciplinary Optimization,* vol. 21, pp. 159-163, 2001.

[62]   E. Holmberg, B. Torstenfelt, and A. Klarbring, "Stress constrained topology optimization," *Structural and Multidisciplinary Optimization,* vol. 48, pp. 33-47, 2013/07/01 2013.

[63]   C. Zillober, "A globally convergent version of the method of moving asymptotes," *Structural Optimization,* vol. 6, pp. 166-174, 1993.

[64]   M. Faragalli, D. Pasini, and P. Radzizsewski, "Multi-objective optimization of a segmented lunar wheel concept," in *ASME 2011 International Design Engineering Technical Conferences and Computers and Information in Engineering Conference, IDETC/CIE 2011, August 28, 2011 - August 31, 2011*, Washington, DC, United states, 2011, pp. 463-470.

[65]   T. Y. Chen and S. C. Wu, "Multiobjective optimal topology design of structures," *Computational Mechanics,* vol. 21, pp. 483-492, 1998.

[66]   V. J. Challis, A. P. Roberts, and A. H. Wilkins, "Design of three dimensional isotropic microstructures for maximized stiffness and conductivity," *International Journal of Solids and Structures,* vol. 45, pp. 4130-4146, 2008.

[67]   V. J. Challis, J. K. Guest, J. F. Grotowski, and A. P. Roberts, "Computationally generated cross-property bounds for stiffness and fluid permeability using topology optimization," *International Journal of Solids and Structures,* vol. 49, pp. 3397-3408, 2012.

[68]   M. T. Juan, J. H. Scott, C. Tien Min, M. S. Rachel, and L. Cheng-Yu, "Design and Fabrication of Bone Tissue Engineering Scaffolds," in *Bone Tissue Engineering*, ed: CRC Press, 2004, pp. 167-192.

[69]   A. Vigliotti and D. Pasini, "Mechanical properties of hierarchical lattices," *Mechanics of Materials,* vol. 62, pp. 32-43, 2013.

[70]   A. Vigliotti and D. Pasini, "A multiscale approach to assess the effect of multilevel structuring on the properties of hierarchical lattice materials," in *2011 MRS Fall Meeting, November 28, 2011 - December 2, 2011*, Boston, MA, United states, 2012, pp. 1-6.

[71]   T. R. Faisal, A. D. Rey, and D. Pasini, "Hierarchical microstructure and elastic properties of leaf petiole tissue in Philodendron melinonii," in *2011 MRS Fall Meeting, November 28, 2011 - December 2, 2011*, Boston, MA, United states, 2012, pp. 67-72.

[72]   T. R. Faisal, A. D. Rey, and D. Pasini, "A multiscale mechanical model for plant tissue stiffness," *Polymers,* vol. 5, pp. 730-750, 2013.

[73]   Q. Chen and S. Huang, "Mechanical properties of a porous bioscaffold with hierarchy," *Materials Letters,* vol. 95, pp. 89-92, 2013.

[74]   H. Rodrigues, J. M. Guedes, and M. P. Bendsoe, "Hierarchical optimization of material and structure," *Structural and Multidisciplinary Optimization,* vol. 24, pp. 1-10, 2002.

[75]   P. R. F. Pedro G. Coelho, José M. Guedes and Hélder C. Rodrigues, "Hierarchical optimization of the structure and the material used in its manufacture," *Mecánica Computacional,* vol. XXIX, pp. 405-415, 2010.

[76]   F. R. A. J. Rose, M. M. C. G. Silva, L. A. Cyster, J. J. A. Barry, X. B. Yang, R. O. C. Oreffo, *et al.*, "The effect of anisotropic architecture on cell and tissue infiltration into tissue engineering scaffolds," *Biomaterials,* vol. 27, pp. 5909-17, 12/ 2006.

[77]   A. L. V. Coelho, E. Fernandes, and K. Faceli, "Multi-objective design of hierarchical consensus functions for clustering ensembles via genetic programming," *Decision Support Systems,* vol. 51, pp. 794-809, 2011.

[78]   P. G. Coelho, P. R. Fernandes, H. C. Rodrigues, J. B. Cardoso, and J. M. Guedes, "Numerical modeling of bone tissue adaptation--a hierarchical approach for bone apparent density and trabecular structure," *J Biomech,* vol. 42, pp. 830-7, May 11 2009.

[79]   G. I. N. Rozvany, "A critical review of established methods of structural topology optimization," *Structural and Multidisciplinary Optimization,* vol. 37, pp. 217-237, 2008.

[80]   I. Synthes, "Small fragment locking compression plate (LCP) system. Stainless steel and titanium.," D. Synthes, Ed., ed, 2002.

[81]   A. J. J. G. R. Thakur, "Anand J.; Thakur; MS (Ortho), FCPS, D Ortho; The Elements of Fracture fixation; 1997; Churchill Livingstone Publisher; New York; 185; Paper Back. ISBN 0443055475," *MJAFI Medical Journal Armed Forces India,* vol. 59, pp. 80-80, 2003.

[82]   M. N. Kumar, V. P. Ravindranath, and M. Ravishankar, "Outcome of locking compression plates in humeral shaft nonunions," *Indian J Orthop,* vol. 47, pp. 150-5, Mar 2013.

[83]   M. Y. Wang, X. Wang, and D. Guo, "A level set method for structural topology optimization," *Computer Methods in Applied Mechanics and Engineering,* vol. 192, pp. 227-246, 1/3/ 2003.

[84]   V. G. Sundararajan, "Topology Optimization for Additive Manufacturing of Customized Meso-Structures using Homogenization and Parametric Smoothing Functions," Master of Science in Engineering, Engineering, The University of Texas at Austin, 2010.

[85]   O. Sigmund, "Materials with prescribed constitutive parameters: an inverse homogenization problem," *International Journal of Solids and Structures,* vol. 31, pp. 2313-29, 1994.

[86]   S. Arabnejad Khanoki and D. Pasini, "Fatigue design of a mechanically biocompatible lattice for a proof-of-concept femoral stem," *Journal of the Mechanical Behavior of Biomedical Materials,* vol. 22, pp. 65-83, 6// 2013.